Natanael F. Hjermann

Mechanical Properties of FDM Manufactured PEEK Components

With Application to Satellites

Master's thesis in Mechanical Engineering
Supervisor: Anna Olsen

August 2022

NTNU
Norwegian University of
Science and Technology

Natanael F. Hjermann

Mechanical Properties of FDM Manufactured PEEK Components

With Application to Satellites

Master's thesis in Mechanical Engineering
Supervisor: Anna Olsen
August 2022

Norwegian University of Science and Technology
Faculty of Engineering
Department of Mechanical and Industrial Engineering

NTNU
Norwegian University of
Science and Technology

Preface

This Master's Thesis was performed at the Department of Mechanical and Industrial Engineering at the University of Science and Technology in Norway. The work was a collaboration between TrollLABS and Kongsberg Defence & Aerospace and was finished in August 2022. It is built on my Project Thesis finished in December 2021. Associate Professor Anna Olsen was my main supervisor.

Abstract

Additive manufacturing, such as Fused Deposition Modeling (FDM), allows for complex geometries. However, challenges in simulating the mechanical properties can hinder its widespread use. This thesis uses Digital Image Correlation (DIC) and uni-axial load testing to estimate the anisotropic properties of PEEK composite infused with 30% carbon fibre. The estimated properties are then used in simulations to compare and validate the accuracy of the test method. Cyclic load testing was also performed due to its relevance for FDM printed satellite components. In addition, the modelled material is used in a Topology Optimization (TO) process to explore what effects anisotropic properties have on the TO process. The method and results can be used to improve the understanding of FDM printed parts with application to satellites.

Sammendrag

Additiv tilvirkning, som Fused Deposition Modeling (FDM), muliggjør for komplekse geometrier. Men, vanskeligheter under simulering av de mekaniske egenskapene kan hindre opptaket. Denne oppgaven bruker Digital Image Correlation (DIC) og strekktesting for å estimere de anisotropiske egenskapene til PEEK med 30% karbonfiber. De estimerte egenskapene blir så brukt i simuleringer for å sammenligne og validere nøyaktigheten til metoden. Syklisklasttesting blir også utført grunnet dens relevans for FDM-produserte satellittkomponenter. I tillegg blir det modellerte materiale brukt i en Topologioptimaliseringsprosess for å utforske hvilke effekter de anisotropiske egenskapene har på prosessen. Metoden og resultatene fra oppgaven kan blir brukt til å forbedre forståelsen av FDM-printede deler til bruk i satellitter.

Table of Contents

List of Figures

List of Tables

1   Introduction

The space sector has experienced a resurgence in the past decade, with multiple new launch providers entering the market [1]. At the same time, advanced manufacturing techniques such as Fused Deposition Modeling (FDM) have become more commonplace and developed further. Using FDM manufacturing in combination with Topology Optimization could drastically reduce the lead time for new components through part consolidation, and fewer machining operations [2]. This could, in turn, allow for the creation of more custom parts depending on the specific mission requirements, relying less on standard components.

However, fundamental mechanical properties must be investigated before FDM can be widely used in satellites. This thesis will focus on how to determine those key properties for PEEK with short carbon fibre reinforcements. PEEK is a strong polymer with low outgassing and a relatively high glass transition temperature, making it suitable for space applications. The same workflow can be duplicated for other filament materials as well. In addition, Topology Optimization will be used and evaluated to see if it can be used successfully in conjunction with the anisotropic properties of FDM printed parts.

The thesis will introduce important information about satellites and other relevant theory regarding FDM printing and Topology Optimization. It will then continue with key mechanical properties pertinent to space applications and how this thesis will determine them. The results will then be presented and analyzed to be used in a Topology Optimization process. Finally, the use of FDM printed PEEK with short carbon fibre for space applications will be discussed.

1.1   Scope and Objections

This thesis aims to provide helpful information to a company wanting to explore using PEEK components manufactured using FDM for satellite components. It will not look at how to optimize the mechanical properties of a material by changing the print settings, such as print speed and infill pattern. Instead, it will focus on how to measure the material properties and then implement them into the simulation and modelling software Ansys for topology optimization. While multiple programs offering topology optimization exist, this thesis will only look at the implementation given in Ansys.

Objectives

- Design a set of test specimens that allow for the determination of mechanical properties;

- Design the experimental procedure to determine the mechanical properties;

- Use the results to model the mechanical properties as a custom material in Ansys;

- Give a characterization of PEEK using FDM, what are the benefits and challenges of using it.

1.2   Limitations

One of this thesis's key limitations is the limitation on machines capable of printing PEEK. In this thesis, only one non-commercial printer is used, meaning the same print settings and qualities might not be obtainable by different parties. The printer is, at the same time, not a finished product, and while a lot of effort has been made to ensure a consistent printing environment, it is not guaranteed the same way a commercial printer could offer.

1.3 Research questions

- How can FDM be used in the production of satellite components;
- How can topology optimization be used together with FDM;
- How can we better understand the properties of components produced using FDM.

1.4 Approach

The workflow that this thesis will follow is the green part of Figure 1. As explained in the scope of this thesis, the step of optimizing the print settings will not be performed. This, however, is relevant if this workflow is to be performed operationally.
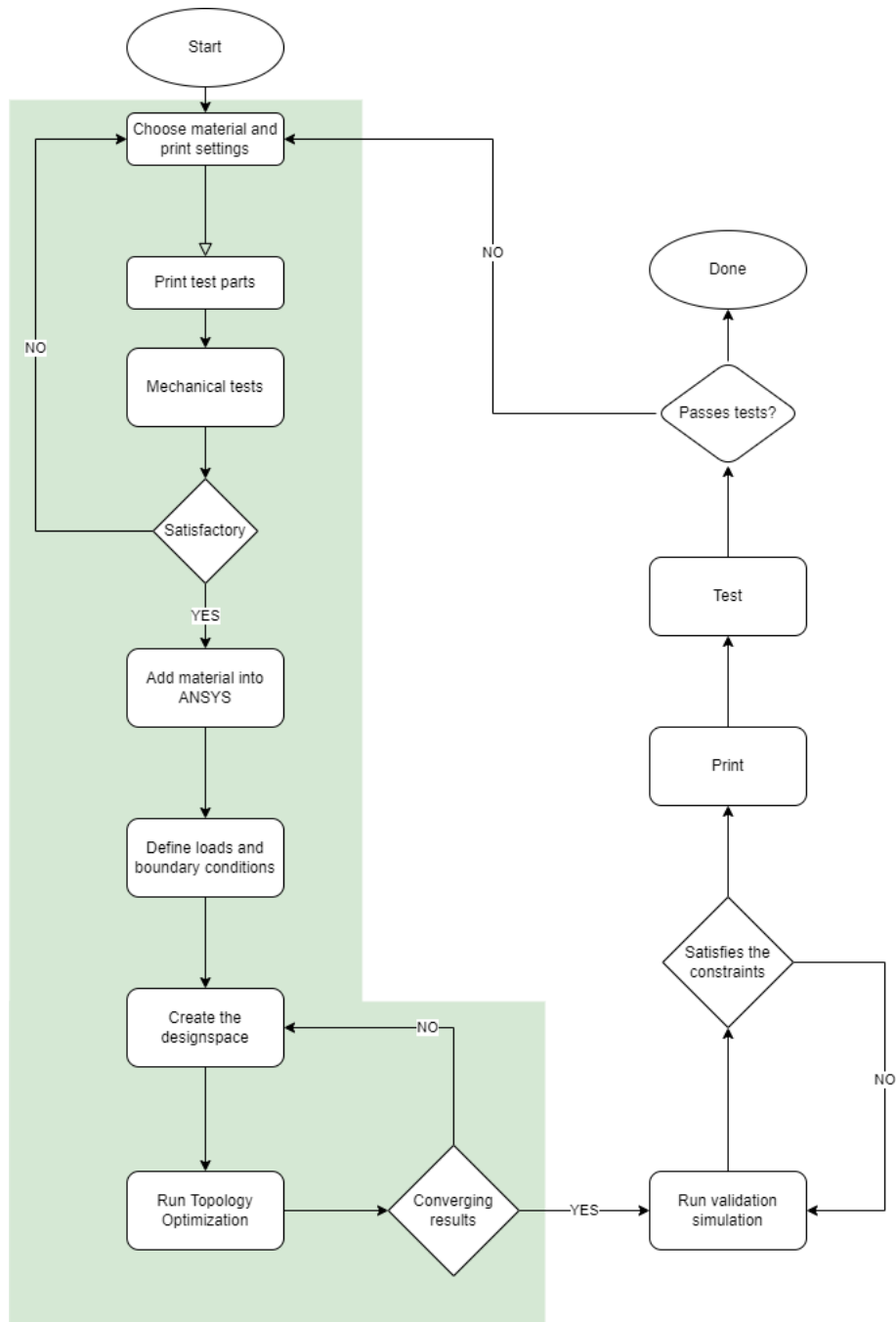
Figure 1: The workflow. The green part is followed in this thesis.

2   Theory

2.1   Satellites

Satellites are objects that orbit a larger celestial body, such as the Earth. Artificial satellites can range in size from just a few centimeters to several meters (Figures 2a and 2b respectively). All artificial satellites need to be launched from Earth using rockets. The price of launching a satellite is largely based on the mass of the satellite, not the size. While all rockets have a volume restriction the mass of the satellite determines the price of the launch, lower mass means less fuel is required. The price pr. kg is in the range of $3000-10000. This provides an incentive to reduce the mass as much as possible to decrease the launch cost.
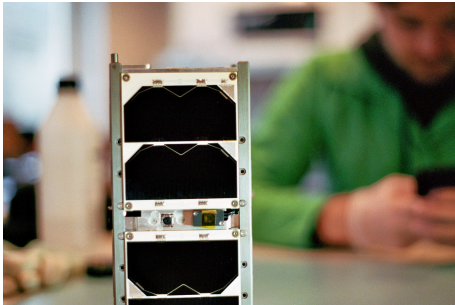
(a) Picture of the SelfieSat Cubesat measuring 20x10x10cm and having a mass of 1.8kg.

(b) A picture of the satellite Viasat-1 with a mass of 6700kg. *https://www.viasat.com/space-innovation/satellite-fleet/viasat-1/*

Figure 2: Pictures showing the range in size artificial satellites can have.

2.1.1   Orbits

An orbit is the curved path an object takes around a different object. Well-known examples of orbits are the Earth's orbit around the Sun, and the Moon's orbit around the Earth. To properly define an orbit around a larger body six parameters are needed. They are as follows: Inclination, Longitude of the ascending node, Argument of periapsis, Eccentricity, Semimajor axis, Mean anomaly at epoch [3]. However, similar orbits around the Earth can be classified based on their height above the Earth and their inclination.

Inclination   The inclination is one of the key parameters needed to define an orbit (Figure 3). An orbit with a 0°inclination will always pass over the equator. While an orbit of 90°results in a polar orbit, where the satellite passes over the poles on each orbit. If the orbit has an inclination of, for example, 20°the furthermost point the satellite will go north and south is 20°. This means if a ground station on Earth located in Paris wants to communicate with a satellite, the satellite will have to have an inclination of at least 48°, the latitude of Paris. Since the Earth is rotating launching satellites from the equator and directly eastwards requires the least amount of fuel to reach orbit. As a result, many satellites have a low inclination orbit. Orbits with a low inclination are called "equatorial orbits" or "near-equatorial orbits".
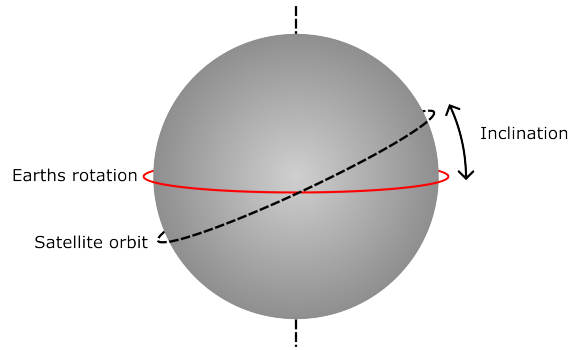
Figure 3: Image describing inclination.

Polar orbits are orbits with an inclination of 90°. Due to the rotation of the Earth, a polar orbit gives the illusion of the satellite moving westwards for each pass. In reality it is the Earth that is rotating beneath it. This can be beneficial if the objective of the satellite is to image every part of the Earth, an equatorial orbit will only give the satellite a view of the land directly around the equator. For this reason most Earth imaging and other Earth observation satellites use a polar orbit. A set of orbits similar to polar orbits are Sun-synchronous orbits (SSO). With SSOs the solar time of the piece of Earth directly underneath the satellite will stay constant during each orbit, only changing between AM and PM. The key benefit of this is that the ground's shadows are constant, and if the satellite passes over the Earth at 12:00 and 00:00 this means no shadows, which is helpful for imaging satellites.

Semimajor axis The other key orbital parameter is the orbital height. For circular orbits (no eccentricity), this is the same as the semimajor axis minus the radius of the Earth. It is normally divided into Low Earth orbit, medium Earth orbit, high Earth orbit and geosynchronous orbits. Orbits with an orbital height of up to 2,000km are defined as LEO. From 2,000km to 35,786km are MEO. Orbits with exactly 35,786km are geosynchronous (GSO or GEO). While orbits above 35,786km are HEO.
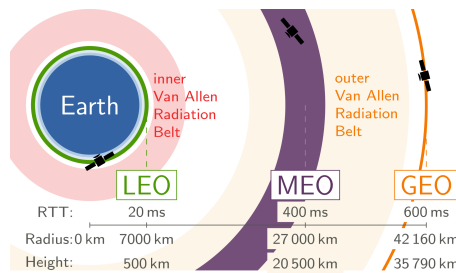
Figure 4: Figure showing the different orbit classifications based on height, not to scale. *Sedrubal, CC BY-SA 4.0 https://creativecommons.org/licenses/by-sa/4.0, via Wikimedia Commons*

The orbital height directly affects the orbital period, the time it takes to complete a full orbit. Lower orbits have a shorter orbital period. This is important because if the satellite needs to point something at the ground, such as a camera or an antenna while pointing its solar panels at the Sun it will have to change the orientation faster the lower the orbital period is. A satellite in geostationary orbit would, for example, only need to rotate its solar panels once per day, while a satellite in low Earth orbit would need to do the same every 90 minutes. The orbital height also affects how much of the ground is in line of sight and the communication delay. Depending on the purpose of the satellite different heights are chosen. Equatorial orbits with higher orbital heights are also in view of the Sun for a more significant portion of the orbit, leading to higher temperatures.

2.1.2 Environment

Launch   During the launch the satellite is exposed to high accelerations and significant vibrations. These are in the range of 10s of Gs [4]. The desire to reduce the mass is therefore met with the need for robust structures. A key aspect of the launch is the vibrations. While each launch vehicle performs differently, it is always necessary for the satellite to have its resonance frequency above a certain frequency. This provides a challenge when designing satellite components, as creating larger and more robust parts might inadvertently push the resonance frequency below the minimum threshold.

The launch itself is generally about 10 minutes long [4]. Most of the vibrations happen in the first part of the launch as the rocket moves through the atmosphere. Depending on the desired orbit, the rocket might have to fire its engine multiple times to get to the correct orbit.

Operation   After the launch and early commissioning, when diagnostics are performed to calibrate sensors and check that all the systems are working as intended, the satellite is in its operational phase. The duration of this phase varies considerably based on the purpose of the satellite, some research satellites might only stay in orbit for a few months to a single year, while other larger communication satellites in GEO might stay for several decades [5]. In the operational phase, the main loads on the satellite are the cyclical loads due to rotating solar panels, communication antennas and other equipment with a specific pointing direction. Depending on the orbit, the satellite can also experience cyclical thermal loads as the satellite enters and escapes the shadow of the earth. Different parts of the satellite will heat up at different rates causing thermal stresses.

Most satellites also feature some way of changing their attitude, their orientation. In the lower orbits drag is present, and in higher orbits drag has less of an effect but the uneven reflection of sunlight will eventually give the satellite an uncontrolled spin. To combat this most satellites use a combination of reaction wheels, small thrusters and magnetorquers to change their rotation. All of these will induce a moment in the satellite, thus loading the inner structure, however in most cases the amplitude and frequency of these loads are small enough to be negligible.

2.2   FDM manufacturing

Fused Deposition Modeling is a common additive manufacturing method (Figure 5). It is characterised by extruding material out a nozzle, fusing it in the desired shape [6]. While FDM can create many shapes, some not possible with traditional machining [2], there are some key points of concern. The mechanical properties are often heavily dependent on the print direction, meaning the strength in one direction is not the same as in another. The prints are also often relatively coarse, which can hinder the cyclic performance. Support material is also sometimes needed depending on the desired geometry [6], the material has to be removed after the printing process, which is time-consuming as it often has to be done by hand.
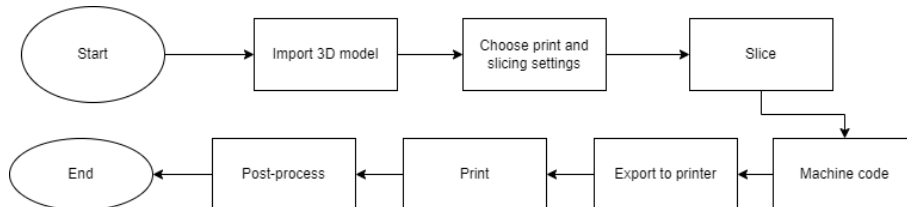

Figure 5: The basic flowchart showing the steps of using an FDM printer.

2.2.1 The printing process

An FDM printer works by heating the filament in the hot end, then extruding the material onto the print bed, or on previously extruded material, in the desired shape (Figure 6). This happens in layers. After finishing one layer the hot end is moved up a fixed amount. When extruded, the filament is in a semi-liquid state that allows the filament to fuse to the previously deposited material [7]. The temperature of the material determines the quality of the fusing, if both materials were completely molten the fusing would be complete. However, if that were the case the deposited material would not retain its shape. Because of this the bonds between layers and between each extruded line are not as strong as one continuous line of material. This is the main reason for the anisotropy in FDM printed parts.
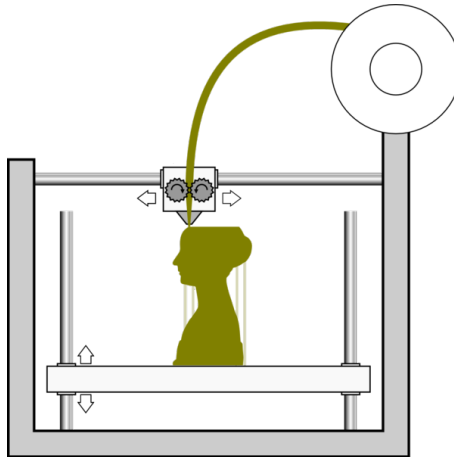
Figure 6: Figure showing the FDM printing process. *Paolo Cignoni, CC BY-SA 4.0 via Wikimedia Commons*

2.2.2 Slicing

A vital aspect of the FDM process is the slicing of the 3D model. 3D model file types typically used in CAD software cannot be directly sliced. Usually, it has to be converted into a triangle mesh filetype called STL [8]. The CAD software generally does this. Before the model can be printed it has to be divided into several layers. While it is possible to print using nonplanar deposition [9], setting a fixed distance between the layers is more common. Each layer corresponds to the model's cross-section at a certain height. The 2D layers are then processed into a set of lines, which the machine follows when depositing the material in the manufacturing step [7]. Several settings can be adjusted for the slicing step, mainly concerning the printing process and the physical properties of the printer. Once the part has been sliced, machine code that is readable by the FDM printer is generated called GCODE.

2.2.3 Dimensional quality and resolution

Because FDM printers deposit materials using a fixed nozzle, the smallest resolution the part can have is determined by the nozzle diameter. As a rule of thumb extrusion widths should be between 100% and 140% of nozzle diameter, but it could go as far as 60-200% [10]. The machine's compliance can also affect the quality of the print. A flexible machine can have problems following the sliced path if the printer head is moving fast due to the momentum of the parts. The layer height also affects the surface quality in the Z-direction, as seen in Figure 7. The effect on the surface quality depends on the angle of the surface. If the angle is close to 0 °from the vertical the effect is minimal, while larger angles give a larger effect. Values for the the layer height are normally 25-75% the nozzle diameter [11]. Lower layer heights affect the printing time a great deal simply because more layers have to be printed.
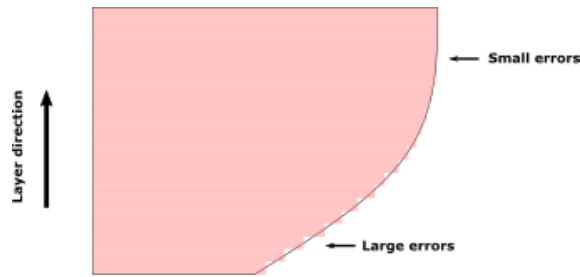
Figure 7: Figure highlighting the effect layers have on vertical surface quality.

2.2.4 Infill

FDM printers can only print lines, they can be curvy but they have a constant, and small, width. The individual slices can be filled using many patterns (Figure 8). The simplest is a rectilinear infill, where the area is filled using straight lines going at 90°angles relative to each other. There are many different patterns, and each will affect the strength of the final part [12]. For example, the rectilinear pattern performs worse than Gyroid, but better than the Concentric pattern. These effects can also differ based on the direction of the stress, a pattern can be much stronger in one direction than another.
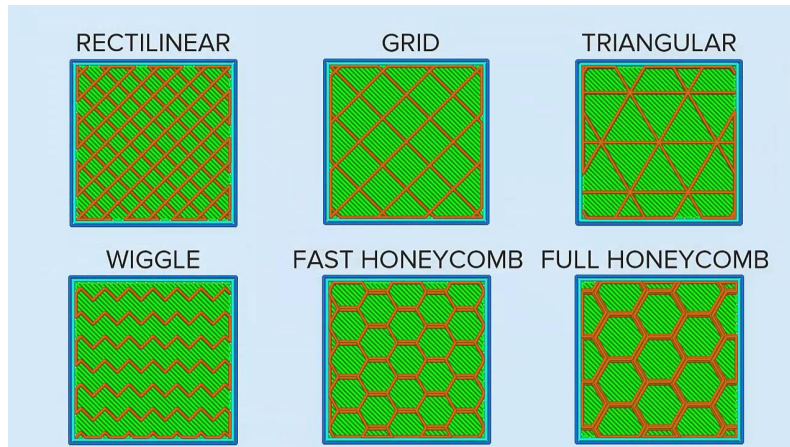
Figure 8: Examples of infill patterns.

3D models are usually solid, meaning the inside of a part is without any empty space. However, FDM allows parts to have empty space in the middle, be completely solid, or have something in between. This is controlled by the infill percentage setting when slicing the part. An advantage of having a semisolid part is that sometimes the geometry is not constrained by the strength of the component but rather some other geometrical constraint, a minimum thickness for example. In those cases, using a lower infill can reduce the mass of the component without compromising the mechanical strength.

2.2.5 Support structures

As with many other additive manufacturing processes, FDM cannot add material when no material is underneath (Figure 9). However, due to the thickness of the deposited material, it can generally be printed at angles up to around 45%. After that, support structures are needed for the printing process not to fail. The addition of support material will increase the time of the print, and it can decrease the part's surface finish. Support structures should therefore be avoided when possible. The best way to do this is to be mindful of overhangs when designing the original part and designing around it. This, however, is not always possible due to other constraints. Using a

different material for the support structure could be advantageous if the printer supports it. For example, water-soluble materials can be used during the printing process and removed afterwards so that the surface of the remaining part is minimally affected. If that is not possible, support structures using the same material is maybe necessary. The major disadvantage of this is that the support material will often fuse with the "real" part, requiring external tools such as pliers to remove and causing the surface finish to diminish. The slicing program will try to decrease the chance of this happening, but it is rarely 100% effective.

Figure 9: Diagram explaining the need for support structures.

A solid surface is often desired, even when the infill percentage is less than 100%. This is done by having a few perimeter lines following the outside of the part at each layer, and solid layers at the top and bottom. For larger parts, this will have a small effect on the part. However, if the part is thin in any direction these perimeter lines will be a more significant percentage of the part. As a result, even parts with a low infill percentage will in fact have a large percentage of material inside the outline of the part.
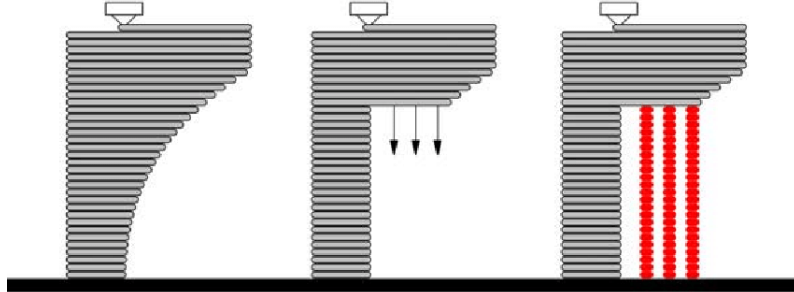
Thin and high parts can also cause problems as the deposition process does put some force on the material underneath. So tall thin structures can bend when the new layer is printed. This will, in the best case scenario, lead to minor geometrical discrepancies. In the worst case, the part can break.

2.2.6 Temperature

The temperature of the previous layer and the current layer being deposited greatly impact the layer adhesion[13]. A higher extruder temperature will, in most cases, increase the layer adhesion, but it can also result in a worse geometrical accuracy simply because the material will flow more. A good cooling system is therefore needed when printing at high extruder temperatures. This will cool the newly deposited material, ensuring its structural ability when printing the next layer. The bed temperature has a less significant effect on the layer adhesion, this makes sense as the bed temperature only affects the lowest layers. Still, having a high enough bed temperature is needed for the first layer to stick to the build plate.

There are other ways of affecting the temperature of the layers, mainly the print speed. If the machine moves quickly, the previous layers have less time to cool down. While the higher temperature is often advantageous, it can get too hot. For example, printing parts with a small cross section area at some features can, in the worst cases, cause the part to fall over during the printing process due to the plastic not solidifying quickly enough. In other cases, this will cause varying layer adhesion throughout the part.

2.2.7 Post processing

Some parts can be used straight from the print bed. However, if support structures were needed they have to be removed. If that is the case sandpapering the surface can also be desired to increase the surface quality[14]. Other forms of post processing include boring out holes to exact dimensions and adding threaded inserts.

The varying temperature while printing can cause internal stresses to appear. A way of mitigating this problem is to heat the parts more uniformly after the printing process and let them cool down gradually.

2.2.8 Simulation challenges

Simulating the mechanical properties of parts produced using FDM is challenging. While the properties of the filament material can accurately be investigated using standard methods, using injection moulded parts for example. As a result, the unique properties of the FDM process are ignored, such as layer adhesion.

As explored in the previous sections, the designer has a lot of choices when printing parts, and all the choices affect the parts' strength. Furthermore, the extent of the effect is not easy to know in advance. This leads to difficulties when trying to predict the performance of printed parts using simulation software.

The main problem when trying to simulate parts is determining the strength and stiffness in different directions. This is heavily influenced by the infill patterns, the print temperature and the print speed. Furthermore, even if these properties are determined for a specific material with a particular set of print settings, the properties will change within the part due to changing surface area and different temperatures of the layer below the print head. These problems do not have a simple solution.

2.2.9 Other Additive Manufacturing Methods

In addition to FDM, many different methods exist for additive manufacturing [15]. Notable examples include selective layer sintering/melting, which allows for the use of other materials such as aluminium, steel and titanium. SLS/SLM also gives a higher resolution due to the use of fine powder and lasers to sinter/melt the desired layers. This, however, comes at an increased cost relative to most FDM printers, and the handling of the materials can be dangerous and difficult as the fine powder can cause health issues if inhaled [2]. As mentioned in the scope of this thesis, the focus will be on FDM and not any other methods.

2.3 Topology Optimization

Topology Optimization (TO) is a subsection of structural optimization. The objective of TO is to optimize the geometry of a part to best fulfil its design goals while adhering to its design constraints [16]. This is achieved using the implementations of different algorithms. The key advantage of TO compared to traditional design, where an engineer designs the part in CAD using a mixture of intuition and simulation to find the best solution, is that the computer can iterate through many different designs rapidly, and it has no preconceived ideas of how the part should be, allowing it to explore more radical designs.

2.3.1 Key concepts

Initial Design To start the optimization process, an initial design has to be created. This design only needs to contain the interfaces to other parts and the places where external loads will be applied. As a result, the initial design is often large and far from the optimal solution.

Design Space The design space is the volume that the algorithm has the opportunity to change the geometry. This volume is defined by the person setting up the Topology Optimization process. In general it is advised to keep the design space as large as possible as this allows the algorithms to explore more designs. Parts of the initial design that should not change need to be kept out of the design space, such as the interfaces to other parts and load points.

Loads and Constraints   Loads and constraints should then be applied to the part. Choosing the loads is up to the designer and requires a good understanding of the environment the part is to be used in. Constraints could be physical requirements such as maximum deflection, fixed surfaces, or maximum stress. Adding a minimum resonant frequency could be a relevant constraint in space applications.

Symmetry around a plane or rotational symmetry is also possible to have as a manufacturing constraint. For additive manufacturing a maximum overhang can be desired. Adding constraints will decrease the number of possible solutions available to the algorithm, which could decrease the effectiveness of the process. It is, therefore, important to only apply necessary constraints so the final design can be as optimal as possible.

Objective Function   The Topology Optimization algorithm will try to optimize the part while keeping within the design space and adhering to the given loads and constraints. To compare the different iterations of designs it creates a "score" for each design. This is done by the Objective Function. This, too, is defined by the engineer based on the use case of the part. Common choices for the objective function are total mass, and stiffness of the part.

2.3.2   Optimization methods

Multiple different algorithms have been developed that solve the optimization problem differently. The various methods will give different results and have unique advantages and disadvantages.

Simplified Isotropic Material with Penalization (SIMP) is a method based on the principle that each small volume of the part is given a value between 0 and 1 [17]. The material constants of that same volume are then modified based on that value. After each iteration the value of each volume is changed to either minimize or maximize the objective function. If the algorithm converges, most of the values will neither be 1 or 0, representing solid or void, so a cutoff value is needed to turn the "semi-solid" part into a part with defined surfaces. However, because this action will change the part's properties, a final simulation has to be done to verify that the finished part meets all the constraints while the given loads are applied.

Level Set is a different method of defining the boundaries of the part in the optimization process [17]. With the Level Set method a level set function gives a value to each point in the design space. If the value is less than 0 the material at that point is considered void, if the value is larger than 0 it is considered solid. During the optimization process, the level set function is modified to optimize the objective function. The advantage of using this method is that each point in the design space is either void or solid, in contrast to the SIMP method. This makes the post processing of the part less ambiguous.

Lattice optimization uses regular cellular structures of varying densities to optimize a part [18]. Instead of changing the boundaries of the part, the internal structure is changed. A way of implementing this method is to use the density values derived from the SIMP approach to determine the density of the cellular structure. A vital advantage of this method is that the outside surface of the part is determined by the designer, and not the algorithm. This can be useful to ensure that overhangs are kept under the desired angle. Challenges arise when trying to predict the mechanical properties of the cells, as they can introduce sources of anisotropy other than the printing process based on the chosen cell type.

Post processing   After the optimization process, the finished part will consist of many thousand small surfaces called a faceted part. It is required to post process the part before it can be manufactured. This is not automatic and the designer has a lot of choices for how to do it. A common way is only to use the results as inspiration, and then design the part from scratch using standard CAD software [16]. This method allows for the parameterization of the part, making it easier to modify the part in the future. The designer will also be able to make simplifications and modifications to make the manufacturing step easier.

Another approach is to take the faceted part and only "clean" the surfaces. This is done by removing faulty facets and unfinished features. Parts destined for manufacturing using AM are most suitable for this "light" post processing as the manufacturing step has fewer constraints.

Validation Simulation Simulations are done for each of the iterations in the optimization step, and the final result, if it converges, should meet all the requirements and constraints. However, the simulations done during the optimization step are simplified, and the final geometry has been changed in the post processing step. As a result a validation simulation has to be performed using the refined model and standard finite element analysis software [19]. If the simulations reveal that the part does not meet the requirements, some manual changes to the geometry could be made, or the optimization step might have to be repeated using different starting settings.

2.4 Digital Image Correlation

Digital Image Correlation (DIC) is a technique that utilizes multiple images of a structurally tested sample to detect changes in the sample. With tensile stress tests the technique is used to accurately and efficiently measure the strain of the sample as it is tested. It works by comparing the patterns of pixels from one image to the next.

The key advantage of this method over, for example, strain gauges is the amount of data that can easily be gathered. With regular strain gauges only one set of data points is collected per strain gauge, strain in one direction at one point. However, DIC allows for estimating the strain in very small areas on the sample and in multiple directions.

To perform DIC the sample needs to be placed in the desired test machine and the sample needs to have a surface with high contrast and a random pattern (Figure 10). The pattern is called Speckle and is used so that the software has reference points to calculate the displacement. If the surface has no contrast, the software cannot differentiate the different points on the surface from each other and can therefore not calculate where they move.
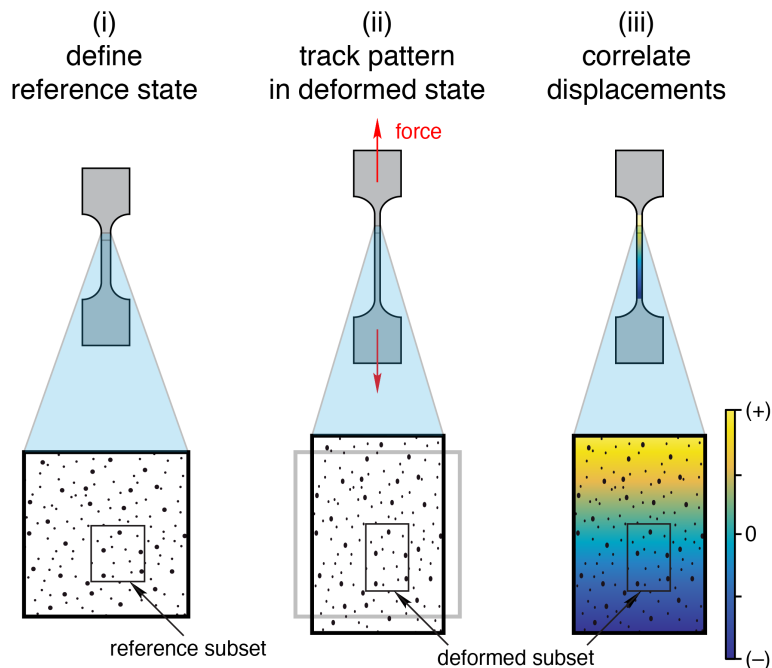

Figure 10: Figure showing the concept behind Digital Image Correlation.

2.5 Anisotropy

Materials can either be isotropic or anisotropic. Isotropic materials are materials that behave in the same way regardless of the direction the property is measured. A typical property that one would want to measure is stiffness. Some materials, such as most metals, have a very isotropic stiffness, the same strain for a given load in one direction as in another direction. If this is not true the material is anisotropic. An example of a naturally occurring anisotropic material is wood [20]. Wood has a higher strength in the direction of the fibres, and a lower strength perpendicular to the fibres. Anisotropic materials are generally harder to simulate and predict, but they can also offer benefits such as having more strength and stiffness only in the necessary directions allowing for lighter constructions. Carbon fibre composites with long fibres in specific directions exemplify this.

$$
\begin{bmatrix} \varepsilon_1 \\ \varepsilon_2 \\ \varepsilon_3 \\ \varepsilon_4 \\ \varepsilon_5 \\ \varepsilon_6 \end{bmatrix} = \begin{bmatrix} S_{11} & S_{12} & S_{13} & S_{14} & S_{15} & S_{16} \\ & S_{22} & S_{23} & S_{24} & S_{25} & S_{26} \\ & & S_{33} & S_{34} & S_{35} & S_{36} \\ & & & S_{44} & S_{45} & S_{46} \\ & & & & S_{55} & S_{56} \\ & & & & & S_{66} \end{bmatrix} \begin{bmatrix} \sigma_1 \\ \sigma_2 \\ \sigma_3 \\ \sigma_4 \\ \sigma_5 \\ \sigma_6 \end{bmatrix} \tag{1}
$$

The general case of anisotropy requires 21 independent material properties to fully explain the deformation during a load, as shown in Equation 1. However, materials with three orthogonal planes of symmetry, an example would be carbon fibre reinforced polymers using fibre mats, can be simplified as an orthotropic material. In those cases symmetry reduces the number of independent elastic constants to 9. Further simplification is possible if the material is considered transversely isotropic. Transversely isotropic materials have a single material direction, for example, the direction of long continuous fibres in a matrix. The material's mechanical properties are isotropic in the plane orthogonal to the material direction. Equation 2 shows the relationship between the stress and strain in such a material. The only independent material constants are the Young's Modulus and Poisson's ratio in the material direction, here labelled E_f and ν_f, and in the direction orthogonal to the material direction, labelled E_t and ν_t, and the shear modulus in the material direction, G_f.

$$
\begin{bmatrix} \varepsilon_1 \\ \varepsilon_2 \\ \varepsilon_3 \\ \varepsilon_4 \\ \varepsilon_5 \\ \varepsilon_6 \end{bmatrix} = \begin{bmatrix} \frac{1}{E_t} & -\frac{\nu_t}{E_t} & -\frac{\nu_f}{E_f} & & & \\ & \frac{1}{E_t} & -\frac{\nu_f}{E_f} & & & \\ & & \frac{1}{E_f} & & & \\ & & & \frac{1}{2G_f} & & \\ & & & & \frac{1}{2G_f} & \\ & & & & & \frac{1+\nu_t}{E_t} \end{bmatrix} \begin{bmatrix} \sigma_1 \\ \sigma_2 \\ \sigma_3 \\ \sigma_4 \\ \sigma_5 \\ \sigma_6 \end{bmatrix} \tag{2}
$$

2.6 PEEK

Polyether ether ketone (PEEK) is a semi-crystalline thermoplastic polymer [21]. Thermoplastics can be remoulded several times and still keep their strength. This is in contrast to thermoset plastics, which once cured cannot be melted again [22]. Thermoplastics are, therefore, the only plastics useful in FDM manufacturing. PEEK material was discovered in 1978 and has multiple mechanical properties that suit it for use in FDM manufacturing and space applications.

PEEK has low outgassing, meaning less of the material will dissipate into the surroundings in a vacuum. This is important in space applications where outgassing can cause contaminants to build up on sensitive sensors, such as imaging sensors. The outgassing properties of PEEK are show in Table 1 [23].

PEEK also offers high strength and a high glass transition temperature, with a tensile strength of 105MPa in injection moulded parts and a glass transition temperature of 143 [24]. The high glass transition temperature gives the material a higher operating temperature.

Table 1: The outgassing properties of PEEK as reported by NASA.

PEEK	TML	WVR
	0.14 %	0.05

2.7 Short fibre carbon composites

Adding short carbon fibres to polymers can be done to change the mechanical properties of the material. The Young's modulus of the fibres are higher than the Young's modulus of the polymer. When the composite is subject to a load some of the load will be transferred through the fibre instead of the polymer chains [22]. The resulting Young's modulus of the material is dependent on the fibre fraction, and it is dependent on the fibre direction in relation to the load direction. When dealing with short fibre composites, the direction of the fibres can often be assumed to be random, and thus the resulting Young's modulus of the material is isotropic. However, in the case of FDM manufacturing, because the material is pressed out of the nozzle the fibres, and the polymer chains, will have a prefered orientation parallel to the extrusion direction. This will cause a higher Young's modulus in that direction[22].

To estimate the Young's modulus of the composite we can use Equation 3 to estimate a higher bound, assuming all the fibres are in the load direction. And we can use Equation 4 to give a lower band of the estimated Young's modulus assuming all the fibres are transverse to the load direction. E_m and E_f represent the Young's modulus of the matrix and fibre used, while f_f is the percentage of fibre in the composite.

$$E_{||} = E_m \left[1 + f_f \left(\frac{E_f}{E_m} - 1 \right) \right] \tag{3}$$

$$E_{\perp} = \frac{E_m}{1 + f_f \left(\frac{E_m}{E_f} - 1 \right)} \tag{4}$$

2.8 Cyclic loading

Cyclic loading is when a part is subject to a varying, repeating load. A common form of cyclic loading is sinusoidal load, where the load varies in intensity over time following a sinusoidal pattern. In that case, the load will reach a maximum, σ_{max}, then a minimum, σ_{min}. Halfway between the maximum and minimum, the load is at the median intensity, σ_{mean}. R is the stress ratio of the cyclic loading. A value of -1 indicates that the mean load is zero, meaning the load perfectly oscillates between tension and compression. σ_A is the amplitude of the load, meaning how much the load varies from the mean. A visual explanation of the concepts can be seen in Figure 11 and the relationship between the different values is explained using Equations 5.

$$R = \frac{\sigma_{min}}{\sigma_{max}} \tag{5a}$$

$$\sigma_{mean} = \sigma_{max} - \sigma_{min} \tag{5b}$$

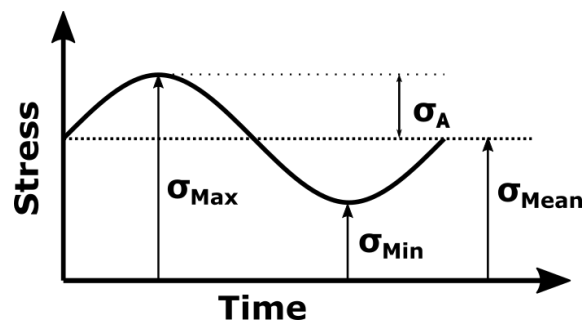$$\sigma_A = \sigma_{max} - \sigma_{mean} \tag{5c}$$

Figure 11: Figure showing the key values in sinusoidal cyclic loading.

3 Key mechanical properties

To use new materials key mechanical properties have to be investigated. Some of these properties are independent of the manufacturing method, such as the density of the material, while others can vary significantly with the method. In the context of FDM printing parts used in the space sector the anisotropic and cyclic properties of the finished part should be investigated.

Anisotropic The anisotropic properties of FDM printed components are essential to investigate as ignoring them can result in unexpected failures. The layer adhesion is seldom perfect, resulting in parts weaker in one direction than another. If this is not expected and accounted for test data obtained from one direction might be used to predict the strength in another. Because the anisotropic properties are a result of the manufacturing process, and not an inherent property of the material, the properties have to be investigated every time the printing settings have been changed.

In this thesis samples will be printed using three different orientations, and then subjected to a tensile load. The Young's modulus, UTS and Poisson's ratio will then be calculated for each orientation.

Effect of support material When printing parts using FDM, support structures are often required for more complicated geometries. As explained in Section 2.2 the support structure will often affect the surface quality where it touches the part. This could negatively affect the strength of the part, and if the effect is large it should be taken into consideration when designing parts, either by accounting for the reduced strength, or adjusting the geometry to remove the need for the support structure.

Cyclic performance Satellite components will experience cyclic loading in all phases of use. During the launch and up to the insertion into orbit the forces from the engine, atmospheric effects, and the volume of the engine's sound will induce a cyclic load on the parts in varying intensity and frequency. During the operation of the satellite in orbit lesser cyclic loads are expected. Still, parts that point in specific directions will, in most cases, experience some form of cyclic loading as the satellite orbits around the Earth. These parts could be Solar Array Drive Mechanisms that have to stay pointing towards the Sun, or antenna pointing mechanisms tracking ground stations as the satellite moves above. Determining the fatigue life properties of the material is critical to ensure that the components do not fail within the planned operation of the satellite.

The launch is, as explained in Section 2.1.2, short so the number of total cycles with high loads are expected to be limited. The cyclic testing done in this thesis will therefore focus on high amplitude loading. The loading frequency during the launch is in the range of 10-100Hz [4] so the tested loading frequency will be withing that range as well. Depending on the part's orientation relative to the launch direction the mean load can be positive, negative or zero.

3.1 Experimental procedure

3.1.1 TECAFIL PEEK VX CF30

Tecafil PEEK VX CF30 is a filament material produced by Ensinger based on their PEEK plastics. It is infused with 30% short carbon fibres. The manufacturers provided properties are shown in Table 2.

It advertises a high strength-to-weight ratio suitable for metal substitution. The carbon fibres give the plastic a higher thermal conductivity, and lower thermal expansion [25]. This is advantageous when FDM printing as it mitigates some of the warping and residual stress problems common in FDM printing. An important point when studying the listed mechanical properties is that even

Table 2: Table displaying key material properties of *Tecafil PEEK VX CF30* provided by the manufacturer.

| Property	Value	Unit
Tensile Strength	190	MPa
Modulus of elasticity	17.5	GPa
Elongation at break	2	%
Glass transition temperature	143	°C
Melting temperature	343	°C
Service temperature (short term)	300	°C
Service temperature (long term)	260	°C
Thermal expansion (CLTE)	4	$10^{-5}K^{-1}$
Moisture absorption	0.03	%
Nozzle temperature	420-460	°C
Print bed temperature	160-230	°C
Build chamber temperature	180-230	°C
Predrying temperature	120	°C
Predrying time	8	hours

though the filament is specifically designed for FDM printing, the properties are obtained using injection moulded specimens. Therefore, obtaining the same results when the parts are 3D printed is not realistic, but they will provide an upper estimate.

3.1.2 Specimens

To investigate the mechanical properties of PEEK-CF30 test specimens had to be designed, manufactured and tested. Because there are no established standards for testing FDM printed parts, selecting the standard was considered carefully. Similar standards used for the testing of plastics and composites do exist, such as ISO 527 [26], however they do not account for the specific challenges related to FDM printing. Previous attempts at using the ISO standard resulted in failed tests, especially when printing vertical samples [27]. Using the advice given by a previous Masters's student, the ASTM E466 [28] standard was chosen as the specimen design due to its ability to be printed vertically without the use of support material. Radius, width and thickness were set at 80mm, 10mm and 5mm respectively. Both specimen specifications can be seen in Figure 12. The same design was used when printing horizontal specimens.
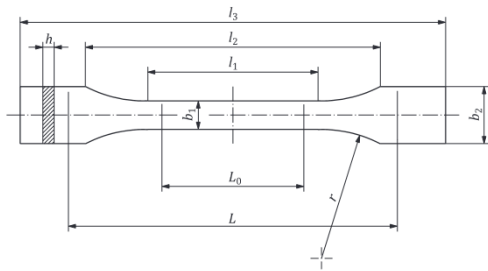
(a) The specification for type 1B specimens as described in ISO 527.
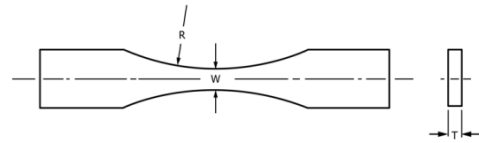
(b) The specification for continuous radius between ends with rectangular cross section specimens as described in E466.

Figure 12: Specimen specifications from ISO 527 and E466.

With the intent of investigating how the mechanical properties of parts printed with PEEK-CF30 change due to orientation, both in build direction and in raster angle, multiple different versions of the specimens were selected. Three different print directions and two different raster angles. The different print directions can be seen in Figure 13. The vertical samples have the load direction parallel to the print direction, so the load is transferred using interlayer bonding. Two versions of the horizontal specimens were choosen. In both versions the load is transverse to the print direction, however in one version the print direction is the thickness direction and in the other, it

is in the width direction. They are called horizontal and horizontal rotated respectively.
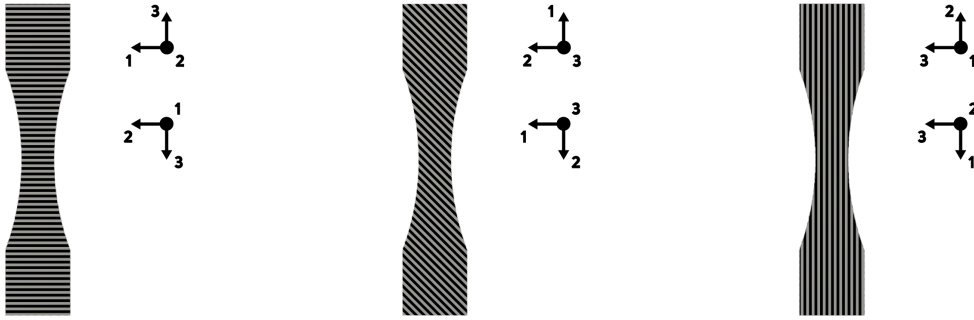
(a) Figure showing the geometry and orientation of the vertical part when printed.

(b) Figure showing the geometry and orientation of the horizontal part when printed.

(c) Figure showing the geometry and orientation of the horizontal and rotated part when printed.

Figure 13: The orientations of all the parts when printed.

The rotated samples would, in a simplified world, give the same results as the horizontal samples, due to the raster pattern being rotationally symmetric every 90°. However due to effects such as printer speed, layer temperature and support material the strength could be affected significantly as explained in Section 2.2. It was therefore considered pertinent to include this type of specimen. For the rotated specimens, support material was required to print the parts.

3.1.3 The FDM Machine

The machine used to manufacture the specimens is a custom machine based on the CR10 Plus machine [29]. It has later been modified as described in [27]. The machine has a build size of 500x500x500mm and is enclosed in an isolating box. Additional heating elements have been added to operate the printer at high chamber temperatures. Water cooling loops were also added to keep critical parts cool, such as the stepper motors. The printer head was also cooled to prevent the filament from melting in the feeder tube, which would have resulted in clogs and the machine stopping functioning. A picture of the inside of the machine can be seen in Figure 14.

In addition the filament holder is placed in a separate box that allows for the filament to be dried before printing. The software controlling the printer is run on a Raspberry Pi attached to the outside of the chamber, which also hosts a website allowing wireless control of the printer. Through this interface, the GCODE is uploaded and the various printer functions are controlled, such as preheating the chamber and homing the axis.

The printer was chosen because it is the only printer capable of printing PEEK at such high temperatures available at the Mechanical Institute. Commercial printers capable of printing PEEK exist, such as the Apium P220 [30], however the price in the realm of tens of thousands of dollars was a limiting factor for this thesis.

3.1.4 Slicing

Again owing to the lack of standards when testing FDM printed parts, some of the print settings could be chosen at will. However some settings are directly linked to the printing machine and are therefore fixed, these primarily relate to the maximum speed, acceleration and jerk of the print head, as well as the maximum temperatures in the chamber, on the build plate, and in the hotend.
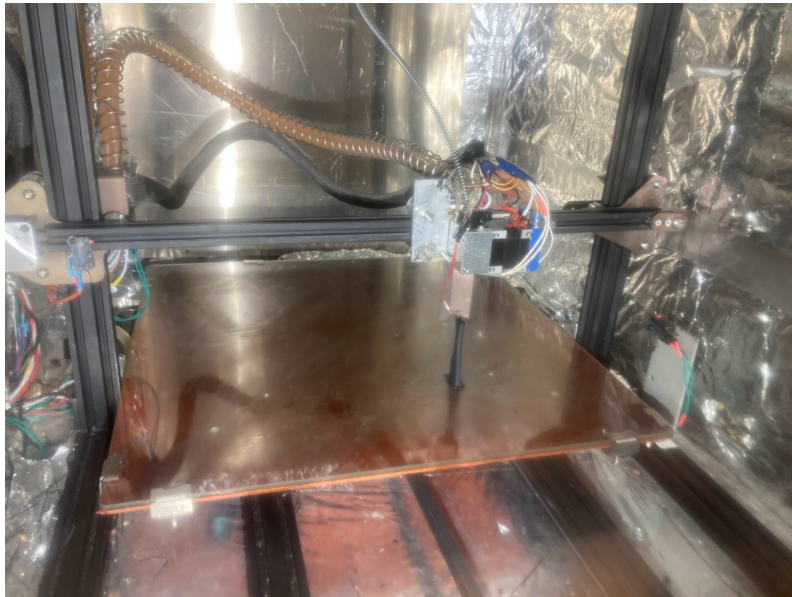
Figure 14: Picture showing the inside of the FDM machine while printing a vertical sample.

Based on results obtained by *Bjørken* [27], a Layer Time Goal of 6 seconds was chosen. The effect of this is that the slicing software manages the print speed based on the layer area so that the entire layer takes 6 seconds. This was shown to give the highest inter-layer strength, and the constant layer completion time gives a more constant temperature when the layer area is changing, ideally giving a more constant inter-layer strength throughout the height of the part.

The temperatures were set based partially on the recommended temperatures in the datasheet provided by the filament manufacturer, and partially by the limitation of the machine. The manufacturer recommended nozzle temperatures of 440°C were achievable in the machine and were therefore used, however the recommended build chamber temperature of 230-250°C was not possible with the printer so a temperature of 90°C was used. This is expected to affect the strength of the specimens. A complete list of the most relevant print settings can be seen in Table 3.

Table 3: Table showing key slicing settings used when printing the specimens.

Property	Value
Perimeters	2
Solid top layers	3
Solid bottom layers	3
Layer height	3mm
Infill	100%
Brim	10mm
Nozzle diameter	0.6mm
Seam position	Aligned
Layer time goal	6 seconds
Max speed reduction	99.99%
Min print speed	1mm/s
Extruder temperature	440°C
Bed temperature	160°C
Chamber temperature	80°C

3.1.5 Manufacturing

Printing the specimens was similar for all the samples and followed a simple procedure. Firstly the filament was kept in a low moisture and high temperature environment for over 24 hours.

This was done to remove any moisture from the filament, resulting in poor quality prints due to water vapour during the printing process. The datasheet recommends a temperature of 120°C for 8 hours, however this was not achievable using the provided printing machine so a temperature of 80°C for a longer time was used instead.

Secondly, the printer was made ready for printing. The print bed was cleaned using water and paper towels. This is done to remove dirt and dust that can reduce the bed adhesion, resulting in parts that get loose, and ultimately fail. The print bed surface is solid glass, and to ensure good bed adhesion, a compound called Magigoo Pro HT was used. The compound becomes more sticky at higher temperatures and was designed with PEEK in mind to reduce the chance of prints accidentally releasing during printing.

The printer was then gradually heated up to the selected printing temperatures. Once the printer was at the correct temperature, the selected GCODE was uploaded to the printer. At the beginning of a printing session a test part was printed to ensure the bed was at the correct height. If it was not, the GCODE was adjusted to compensate for the miss alignment of the build surface.

Then the printing process was started. The printer was left uninterrupted for the duration of the print, however it was checked regularly to ensure no printing errors had occurred. If errors were observed, such as a loss of build plate adhesion or the build plate being miss-aligned, the print was cancelled and the part discarded. Remedies such as adding more Magigoo or adjusting the GCODE were performed before starting the print.

Once the print was successfully done, the printer was opened and the part labelled and stored until further steps. The part number and print settings were also logged in a spreadsheet. The printing process was then started again and new samples where printed until the end of the printing session.

The completed parts were then annealed following the procedure developed by *Bjørken* [27], 200°C for 1 hour, 250°C for 2 hours and then 150°C for 1 hour. This was done to reduce any thermal stress left in the samples after printing.

3.1.6   Post processing

Before the tests could be executed post processing had to be performed on the samples, this is the final step in Figure 5. For these specific samples, the only post processing that had to be done was the removal of support structures for the horizontal rotated parts. Figure 15a shows how the parts looked before the cleaning, and Figure 15b shows how they looked after removal. The removal was done using pliers, as explained in Section 2.2.5 the support material was mostly easily removed, but in a few places it was harder to distinguish between the actual part and the support structure. In Figure 15c it is possible to see how the surface of the sample looked with no support material.

(a) Picture showing the support material on the horizontal rotated specimens.

(b) Picture showing how the horizontal rotated samples looked after the removal of the support structure.

(c) Picture showing the underside of the horizontal rotated specimens after the removal of the support structure. Showing the surface that directly touched the support structure.

Figure 15: Pictures showing the removal of the support material from the horizontal rotated parts.

Due to the intent of using DIC to measure the strain, the samples had to be painted with a speckle pattern. This was done by first applying a thin layer of white spray paint, and then letting the samples dry before applying a "mist" of black spray paint. The black paint was applied from a large distance, approximately 50cm, and the samples were inspected between each spray to see if the optimal speckle density was achieved. This process is inherently not very precise, but care was made to ensure a good density according to the user manual of the DIC software [31].
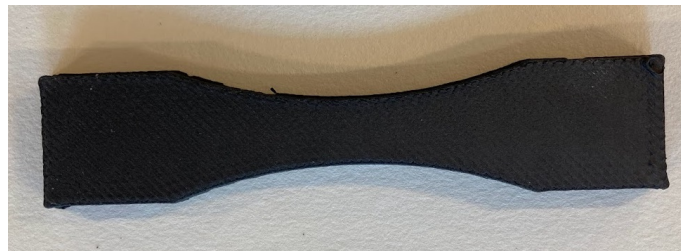
(a) Picture of a horizontal sample before applying the speckle pattern.
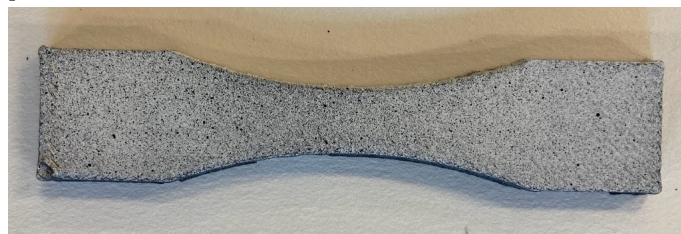
(b) Picture of a horizontal sample after applying the speckle pattern.

Figure 16: Pictures of one of the horizontal samples before and after applying the speckle pattern.

3.1.7 Testing

Tensile testing The tensile testing was done in a *MTS Criterion C42* machine seen in Figure 17a. Each sample was placed in one of the clamps, the load was then zeroed and the second clamp was engaged. The DIC camera started taking photos before any load was applied in order to get a reference image. A picture was taken approximately every 0.2seconds while the sampling rate for the load measurement was 10Hz. Every sample was tested to failure. Once failure occurred the camera was stopped, and the tensile load machine stopped automatically.

Cyclic loading The samples were placed in the cyclic loading machine *Instron ElectroPlus® e10000* seen in Figure 17b. Cyclic stress was the intended test so no strain measurements were done. One side of the sample was clamped first, then the load was zeroed and the other side was clamped. The samples were then given a preload defined by the R number of the test and the maximum stress. Cyclic loading was then started and the number of cycles was recorded until failure.

The vertical $\pm$ 45 samples were tested with a $\sigma_{max} = 95\% - 90\%$ of UTS with a stress ratio of 0.1 and loading frequency of 4Hz in accordance with the tests done by *Bjørken* [27]. This was done to compare the results to verify the process had been completed successfully. The second set of samples, the horizontal 0/90 samples, were tested at varying σ_{max} with a stress ratio of -1 and a loading frequency of 10Hz. Finally, a small portion of horizontal 0/90 samples was tested at the same stress ratio of -1 but only at a σ_{max} of 60% of UTS, due to the limited amount of those samples. This was done to see if there were any major differences in fatigue life between the two raster angles for the horizontal samples.

(a) The tensile test machine used.   (b) The test setup for the cyclic tests.

Figure 17: Pictures of the machines used for the tensile and cyclic tests.

Overview of samples In total 67 specimens were printed. Multiple different settings were used and they were separated into what angle of the rastering was used and the orientation of the samples in the printer, either vertical, horizontal, or horizontal and rotated. A table showing the number of samples in each category can be seen in Table 4. 5 of each sample were intended for tensile testing while extra samples of the vertical and horizontal samples were intended for cyclic

testing. The limitation of filament material restricted the number of samples that were possible to print.

Table 4: Table showing the number of samples printed in each orientation and raster angle.

Total E466 Samples					
67					
±45			0/90		
48			19		
Horizontal		Vertical	Horizontal		Vertical
27		21	14		5
Rotated	Non Rotated		Rotated	Non Rotated	
5	22		5	9	

3.1.8 Analysis of the data

The data collected from the tensile testing is force over time, crosshead extension over time and a series of pictures of the samples over time. The crosshead extension can be used as an approximation of the strain of the sample, however the data also includes the compliance of the testing machine so that data was not used. The pictures were imported to *Vic-2D* where it was analysed following the user guide [31]. The area of the failure was selected as the area of interest (AOI). The software recommended subset and step size was used (67 and 7). Because no absolute extension data was needed no calibration was done. After the analysis of the pictures strain data in the AOI was exported in a CSV file with minimum, maximum, mean, median and standard deviation for the ϵ_{xx} ϵ_{yy} and ϵ_{xy}.

Because the force and strain data were recorded using two separate systems they had to be time calibrated. This was done by finding the point of failure and synchronising that for both data sets. To obtain the stress in the sample the force at any given time was divided by the nominal area of the sample at $50mm^2$.

The data collected from the cyclic testing was simply the maximum and minimum load, and the number of cycles before failure. The load was converted into stress using the nominal area of $50mm^2$.

4 Results

4.1 Tensile Tests

The obtained force and strain data were combined for each sample. Figure 18a shows the raw force and strain data from sample Nr. 21 as an example. The data was then processed into a Stress-Strain graph using the nominal area of $50mm^2$, which is shown in Figure 18b. And finally the Young's Modulus was calculated and plotted as shown in 19. The resulting graphs for all the samples are show in 20.
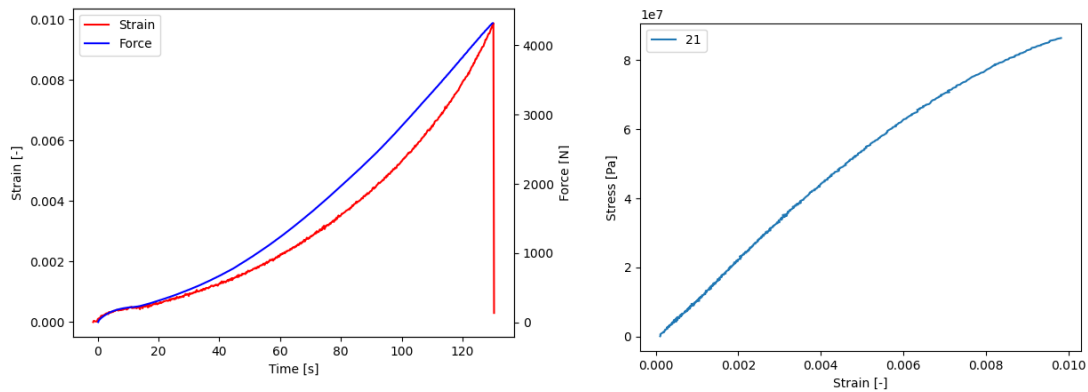
(a) The force and strain data obtained from sample Nr. 21.

(b) The stress strain curve for sample Nr. 21.

Figure 18: Figure showing the raw force and strain data, as well as the computed stress strain graph for sample Nr. 21.
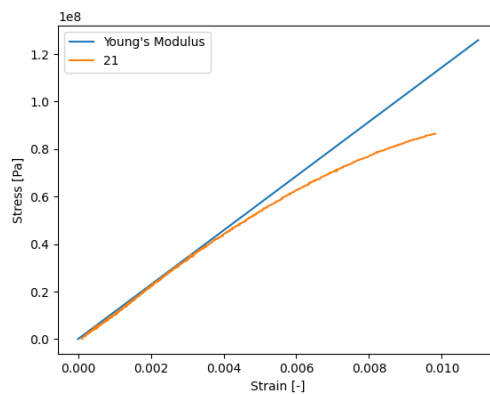
Figure 19: Figure showing the estimated Young's Modulus of sample nr. 21.

From Figure 20 and Figure 21a we can see that the largest difference in Young's Modulus can be attributed to the print direction, either horizontal or vertical. With the horizontal prints being the strongest. A notable exception is the horizontal specimens with a ±45 degree raster, as seen in Figure 20c.

The recorded Young's Moduli are significantly lower than the value stated in the data sheet of $17.5GPa$. The reason for this is that the datasheet values were obtained with injection moulded parts and using higher strain rates, 50mm/min compared to 2mm/min. As commented in Section 2.2.6 the cooling of the layers while printing results in lower inter-layer strength compared to the intra-layer strength. It is therefore expected that the samples where long continuous strands of material are deposited would result in stronger parts. That is observed when comparing the angle
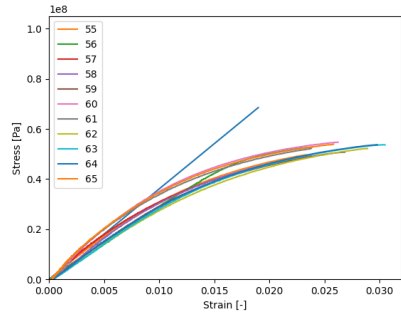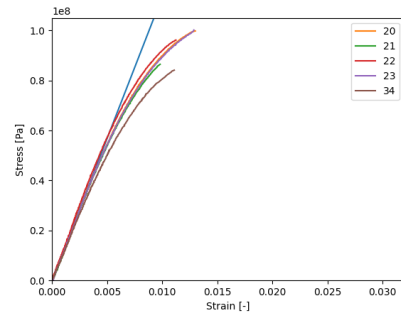
(a) Stress strain graph for the specimens printed in the vertical orientation with ± 45 rastering.
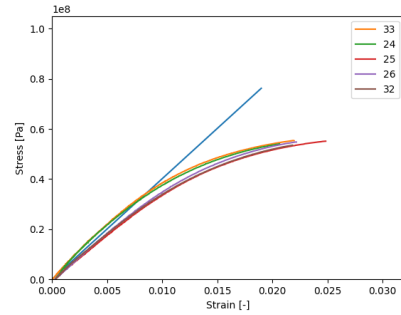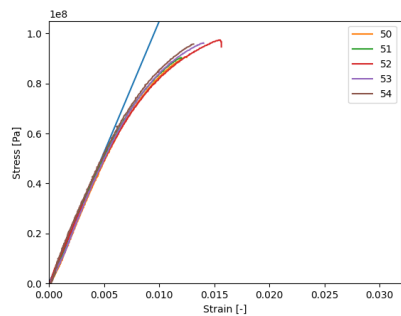
(b) Stress strain graph for the specimens printed in the vertical orientation with 0/90 rastering.
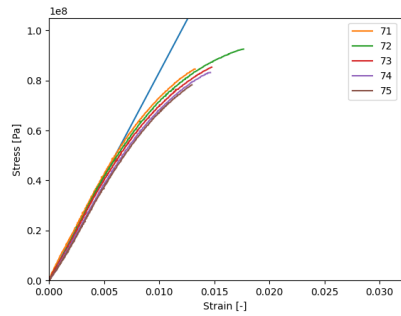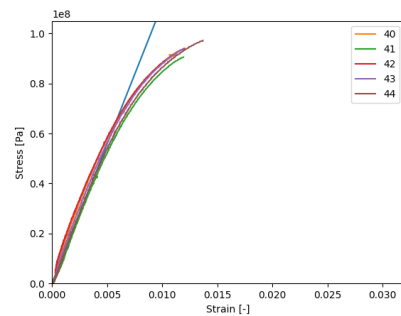
(c) Stress strain graph for the specimens printed in the horizontal orientation with ± 45 rastering.

(d) Stress strain graph for the specimens printed in the horizontal orientation with 0/90 rastering.
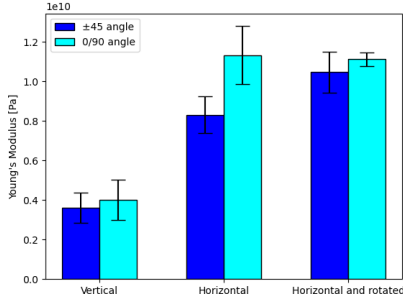
(e) Stress strain graph for the specimens printed in the horizontal orientation with ± 45 rastering, and rotated on its side.

(f) Stress strain graph for the specimens printed in the horizontal orientation with 0/90 rastering, and rotated on its side.

Figure 20: The raw stress strain data from all the tensile tests and the best fit Young's Modulus.
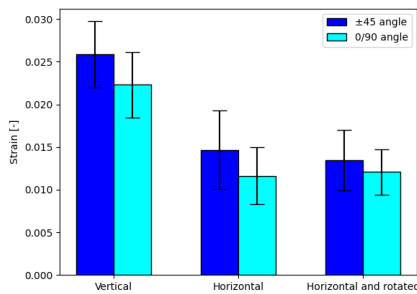
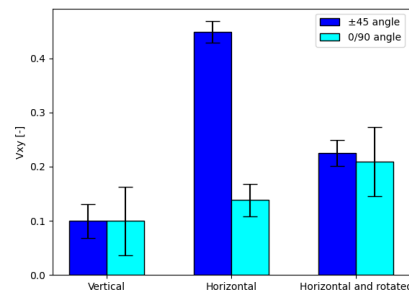(a) The Young's Molduli for each of the sample categories.
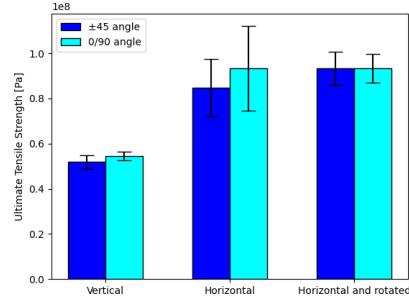
(b) The Ultimate Tensile Strength for each of the sample categories.

Figure 21: The Young's Moduli and UTS for all the samples.

(a) The ultimate strain for all the samples.

(b) The Poisson's ratio for all the samples.

Figure 22: Elongation at break, and Poisson's ratio for all the samples.

of the rasterization, with 0/90 showing a higher Young's Modulus than the ±45 rasterization.

All the failures were brittle, with little deformation before failure. The strain at failure was between 3% and 1%, with the vertical samples having the highest strain and the horizontal samples having the lowest strain. We can also see from Figure 22a that the 0/90 angle samples had a slightly lower average strain at break in all the orientations. Still, in all cases, the 95% confidence intervals overlapped. There are small differences within the horizontal samples, the rotated and non-rotated samples for each raster angle are very similar, indicating that it is the inter-layer bonds that give a larger strain at failure, while the intra-layer bonds give a low strain at failure.

When calculating the strain, the force was divided by the nominal area of $50mm^2$. However due to the varying area of the sample, the break location would affect the total area at that point. In order to control for this the location of the failure was recorded, and a new adjusted stress was calculated based on the more accurate area shown in Figure 23. Here it is clear that the adjusted Young's Modulus is very close to the nominal values in almost all the cases. The only outliers are the horizontal samples printed rotated and with a ± 45 degree rastering angle. This is due to some of the break locations in those samples being further away from the middle than in the other sample categories. The fracture of specimen nr. 54 can be seen in Figure 24a. Here the fracture is not as clean as the one of specimen nr. 51, printed with the same settings, as seen in Figure 24b.
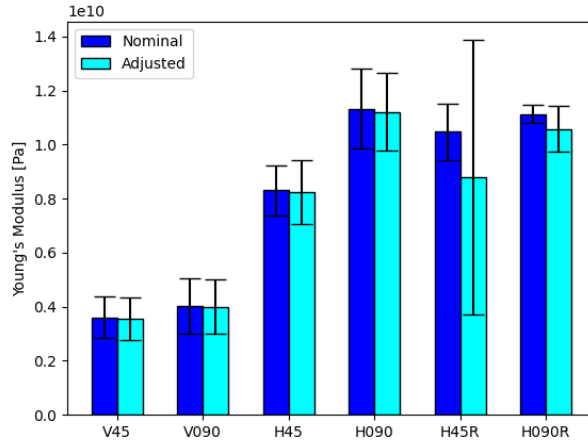
Figure 23: The difference in Young's modulus for all of the sample categories between the nominal area of $50mm^2$ and the more accurate area calculated based on the break location.

(a) Showing the fracture of specimen nr. 54.

(b) Showing the fracture of specimen nr. 51.

Table 5 shows summary of the results.

Table 5: Table showing the Young's Modulus, Yield Stress, UTS and the ultimate strain for each of the categories of samples.

| Name	E [GPa]	Yield Stress 0.2% [MPa]	UTS [MPa]	Strain at break [%]
V45	3.6±0.8	35.4±6.5	51.9±3.0	2.6±0.4
V090	4.0±1.0	41.5±3.6	54.5±1.9	2.2±0.4
H45	8.3±0.9	73.4±7.7	84.7±12.8	1.5±0.5
H090	11.3±1.5	85.9±10.7	93.3±18.8	1.2±0.3
H45R	10.5±1.0	83.1±7.0	93.4±7.3	1.3±0.4
H090R	11.1±0.3	85.7±7.4	93.3±6.5	1.2±0.3

4.2 Cyclic loading

The results from the cyclic loading can be seen in Figure 25. The tests seen in Figure 25a were done to compare the results obtained by *Bjørken* [27], while the other two tests were done to simulate launch conditions better.

From the results we can see that the vertical samples performed significantly better in this thesis compared to the results obtained by *Bjørken*. As the design of the samples, the print settings, the printer and the test parameters were the same this discrepancy has no simple explanation.

When looking at the results from the horizontal fatigue tests we can see that the 0/90 angle samples fail before the ± 45 samples. The difference is however small. When comparing the results between the vertical and horizontal samples it is apparent that the horizontal samples fail much sooner than the vertical samples. The cause is however not obvious as both the stres ratio and load frequency were changed between the two sets of tests. It is therefore impossible to determine what caused the change in fatigue life.

While the temperature of the samples was not recorded, it was noticed that the samples tested at $R = -1$ and a higher frequency of 10Hz were hotter when they failed than those tested at 4Hz at $R = 0.1$. The additional heat could result in the weakening of the material, accelerating the cyclic failure.
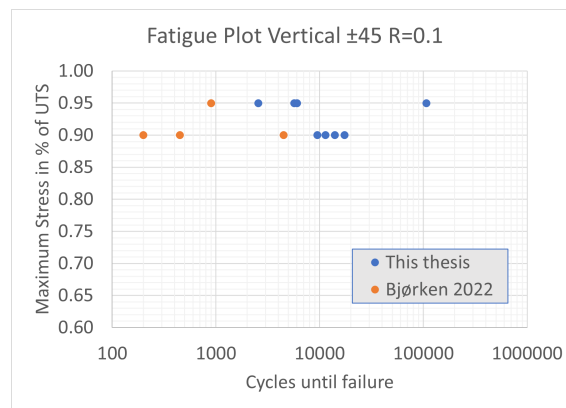
(a) The S-N plot of the vertical ±45 samples, with data obtained in this thesis compared to the data from Bjørken 2022 [27], expressed in percentage of UTS with $R = 0.1$.
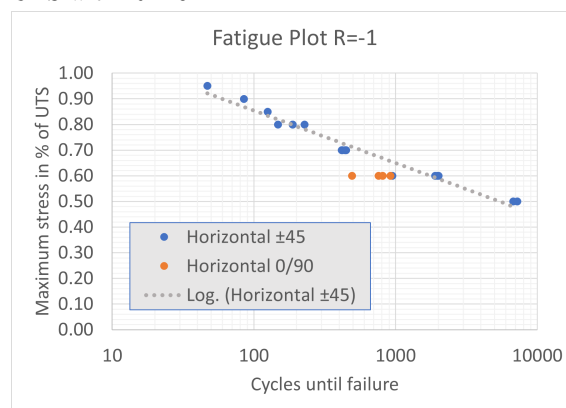
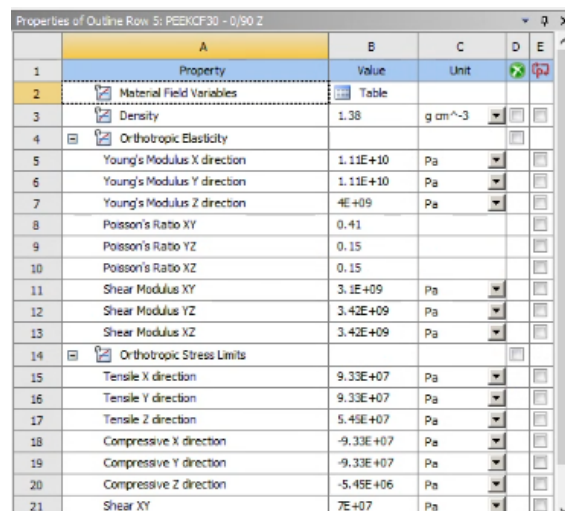(b) The S-N plot of the horizontal samples expressed in percentage of UTS with $R = -1$.

Figure 25: S-N plots of the different samples.

5 Modelling mechanical properties in Ansys

5.1 Creating custom material

Using the results from the tensile tests a custom material was created in Ansys that would try to represent the anisotropic properties of the printed PEEK. Two different materials were created, one for the ±45 degree raster and one for the 0/90 raster.

To accurately simulate the material key mechanical properties had to be defined. The density of the material was taken from the filament datasheet. It was chosen to represent the material as a transversely isotropic material, however as there is no such setting in Ansys the elastic properties of the material were represented as an orthographic material with the properties in the X and Y directions being equal. The values for E_X and E_Y were derived from the experimentally obtained Young's modulus of the horizontal samples, both rotated and non-rotated as seen in Figure 21a. The Poisson's ratio was similarly obtained from the data seen in Figure 22b. Figure 26 shows how the values were input into Ansys. Because no shear tests were performed, the final independent material constant was approximated using the results obtained from a research group based in Bejing [32].


	A	B	C	D	E
1	Property	Value	Unit		
2	Material Field Variables	Table			
3	Density	1.38	g cm^-3		
4	Orthotropic Elasticity				
5	Young's Modulus X direction	1.11E+10	Pa		
6	Young's Modulus Y direction	1.11E+10	Pa		
7	Young's Modulus Z direction	4E+09	Pa		
8	Poisson's Ratio XY	0.41			
9	Poisson's Ratio YZ	0.15			
10	Poisson's Ratio XZ	0.15			
11	Shear Modulus XY	3.1E+09	Pa		
12	Shear Modulus YZ	3.42E+09	Pa		
13	Shear Modulus XZ	3.42E+09	Pa		
14	Orthotropic Stress Limits				
15	Tensile X direction	9.33E+07	Pa		
16	Tensile Y direction	9.33E+07	Pa		
17	Tensile Z direction	5.45E+07	Pa		
18	Compressive X direction	-9.33E+07	Pa		
19	Compressive Y direction	-9.33E+07	Pa		
20	Compressive Z direction	-5.45E+06	Pa		
21	Shear XY	7E+07	Pa		

Figure 26: An example of how the material properties were imported into Ansys.

5.2 Validation of the material

In order to ensure that the results from a Topology Optimization process using the created materials are accurate, the material should be compared to the empirical data obtained. This is done by replicating the tensile test setup in Ansys and comparing the results.

The materials were created using the X-Y plane as the layer plane, and the Z direction as the layer height direction. To replicate the vertical, horizontal and horizontal rotated samples three different models had to be created, each rotated as shown in Figure 27.
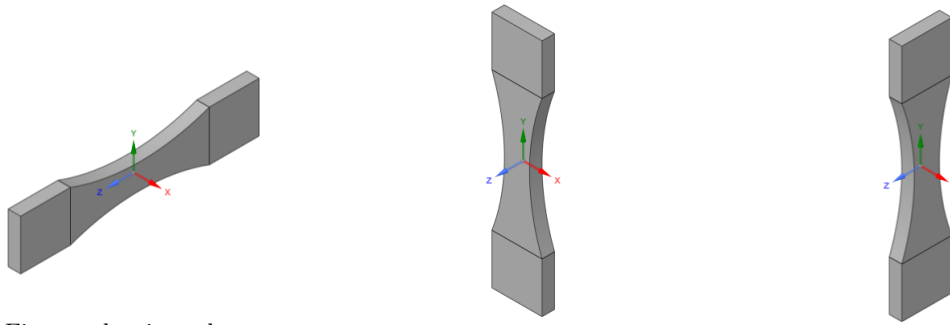
(a) Figure showing the geometry and orientation of the vertical part used for verification simulation.

(b) Figure showing the geometry and orientation of the horizontal part used for verification simulation.

(c) Figure showing the geometry and orientation of the horizontal and rotated part used for verification simulation.

Figure 27: The orientations of all the parts used for the verification simulations of the materials.

Each of the parts is then subject to a 5kN load on one side of the part, and a fixed support on the other, as shown in Figure 28a. Because the strain measurements were done using a rectangle in the centre of the specimen, a similar area was selected when recording the strain data as seen in Figure 28b.

(a) Showing the placement of the 5kN force, section A, and the fixed support, section B, on the vertical validation simulation.

(b) Figure showing where the strain data was recorded from.

Figure 28: Figures showing the location of the force and support, and where the strain data was recorded from on the vertical validation simulation.

Finally, average strain inside the area and the force over time was exported and compared to the data from the physical tests. The comparison can be seen in Figure 29.
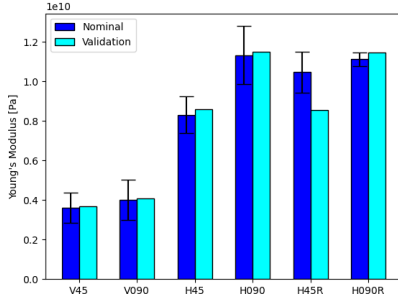
(a) Figure comparing the Young's modulus of the validation simulations to the empirical data.
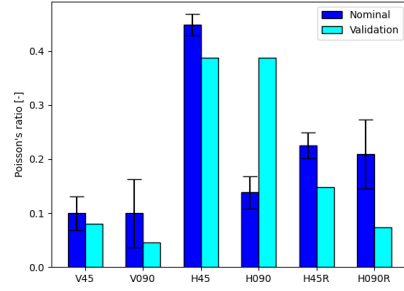
(b) Figure comparing the Poisson's ratio of the validation simulations to the empirical data.

Figure 29: Figures comparing the results from the validation simulations to the empirical data.

5.3 Discussion

The results from Figure 29a show that the validation simulations support the method used to estimate the Young's modulus from the physical tests. From Section 5.1 we recall that the Young's modulus of the virtual material was set to the average measured Young's modulus of the real material, this corresponds to the blue bars in Figure 29. While the difference is small we can observe that the estimated Young's modulus of the validation material is consistently higher than the real material. One possible explanation for this discrepancy is that because only the strain data from a section of the cross section was used, the average strain measured was in fact smaller than the true average strain. A smaller strain for the same amount of stress would give the illusion of a stiffer material. Finally we can observe that the validation material does indeed appear to be transversely isotropic, as the Young's modulus for the horizontal, and the horizontal and rotated orientations show the same Young's modulus.

As for the results in Figure 29b we can see that the measured and validation Poisson's ratios differ hugely from each other. Based on this we can conclude that the methodology does not produce an accurate virtual model of the material. Due to the small absolute displacements when performing the physical tests it is not unreasonable to suspect some of the error originated from the measurement and calculation of the Poisson's ratio. In any case the conclusion is the same, it is not possible to use the virtual material to predict the strains of the printed material accurately.
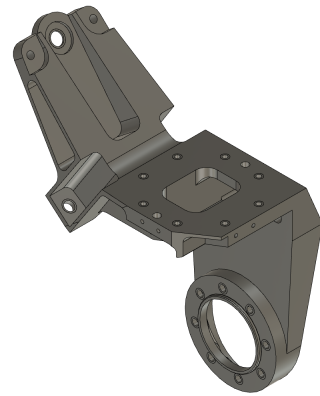
6 Topology optimization

This Section will use the materials created in the previous Section in a Topology Optimization process. The purpose is to investigate if the materials' anisotropic properties will significantly affect the result of the optimization process. The TO process will use two satellite parts provided by Kongsberg, while the loads and constraints will be simplified while still realistic.
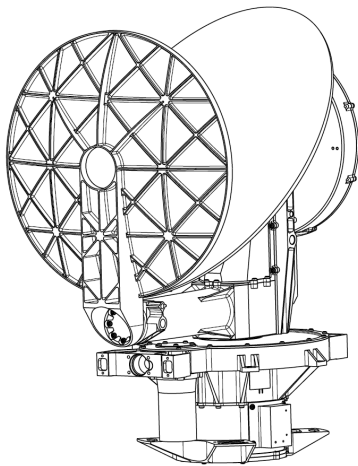
6.1 The problem

Kongsberg Defence & Aerospace produces, among other things, a wide range of antenna pointing mechanisms. Two of these are presented as inspiration for parts used in this thesis. They provide realistic parts to be printed using FDM with PEEK.
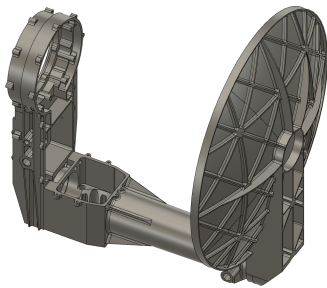
(a) Figure of Part A.

(b) Figure of Part B.

(c) Another view of Part A provided by Kongsberg.

(d) Another view of Part B provided by Kongsberg.

Figure 30: The parts used in the Topology Optimization process.

Part A is fastened to the rest of the satellite at the bottom. On the left-hand side there is a mirror connected to a rotating motor used to change the direction of radio waves that reach the antenna and it can be seen in figure 30c.

Part B is the upper part of KARMA-7 manufactured by Kongsberg. It is also a part of an antenna pointing system, however it is only the upper part. Figure 30d shows a picture of the part. It has an antenna fastened to it, and it is fastened to a rotating motor.

The mechanical requirements are that the structures should be able to withstand accelerations of up to 30g ($294\frac{m}{s^2}$) in any direction. In addition to this the first natural frequency of the structure should be above 100Hz to avoid excessive shaking during the launch.

6.2 Optimization setup

The original parts were simplified and the design space was increased for the initial design. For Part A the two parts were consolidated. Interfaces were represented using larger simplified bodies. In both parts it is possible to use Hold Down Release Mechanisms (HDRM) that add some stiffness to the parts during launch, but that can be released before the parts are to be used. The connections to the HDRMs were modelled using cylinders. The parts also have additional hardware bolted onto the original parts. To simulate this point masses were added and fixed to specific parts of the surface. Figure 31 show how the models used for the TO process looked like.

The parts were constrained physically using a mixture of fixed and cylindrical supports, to simulate being fixed to other components and the HDRM. Uni-axial acceleration of 30g in three orthogonal directions was applied in three separate steps. A modal simulation was then completed to find the natural frequency of the part.

A mass constraint of 60-30% of the original mass was also applied. This requires the topology algorithm to reduce the mass by at least 40%. The natural frequency was constrained to be higher than 100Hz, and the maximum stress was constrained to be 35MPa. While the Ansys software allows for the simulation of anisotropic materials and the definition of separate ultimate tensile stresses for different directions, the topology optimization process only has the option of setting one maximum stress. The maximum stress was therefore set at the lowest yield stress of the material. The objective function of the TO was set to compliance and the topology optimization algorithm chosen was SIMP.

Each part was simulated six separate times, only changing the material and orientation of the part. The change in direction of the part was done to simulate a change in the printing direction. It was decided not to include any overhang constraints due to the samples with support structures not performing significantly worse than those without.
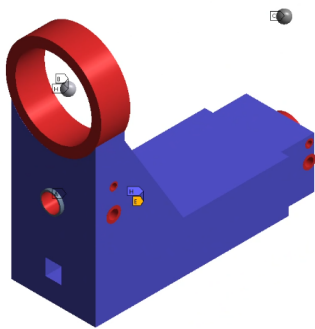
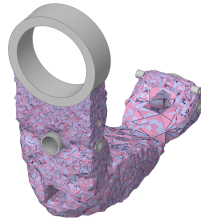(a) Figure showing the model of Part A used in the TO process.
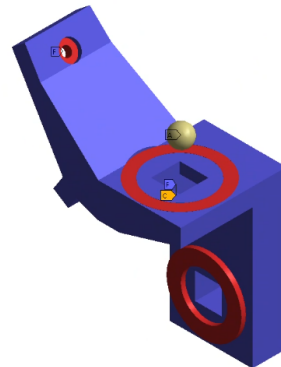
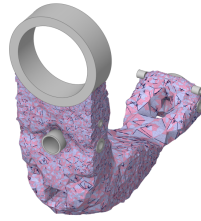(b) Figure showing the model of Part B used in the TO process.

Figure 31: The models used in the TO processes. Blue areas indicate the design space while the red areas show where constraints are placed.
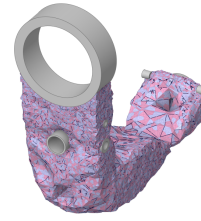
6.3   TO results

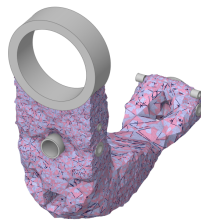The results from the topology optimization can be seen in Figure 32 and Figure 33.

(a) Results from the Topology Optimization process of Part A with ± 45 rastering and X print direction.
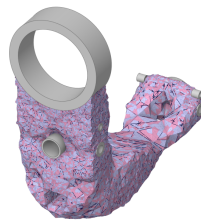

(b) Results from the Topology Optimization process of Part A with ± 45 rastering and Y print direction.
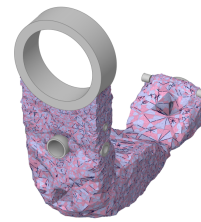

(c) Results from the Topology Optimization process of Part A with ± 45 rastering and Z print direction.

(d) Results from the Topology Optimization process of Part A with 0/90 rastering and X print direction.
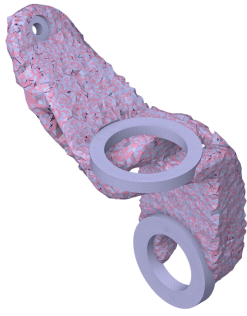

(e) Results from the Topology Optimization process of Part A with 0/90 rastering and Y print direction.
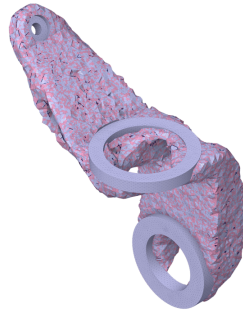

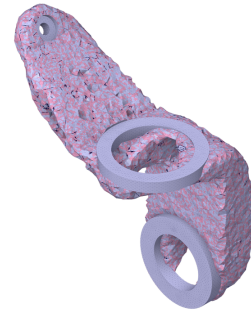(f) Results from the Topology Optimization process of Part A with 0/90 rastering and Z print direction.

Figure 32: The results from the Topology Optimization process of Part A.

(a) Results from the Topology Optimization process of Part B with ± 45 rastering and X print direction.

(b) Results from the Topology Optimization process of Part B with ± 45 rastering and Y print direction.
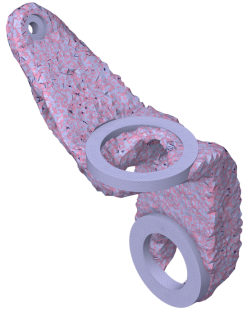

(c) Results from the Topology Optimization process of Part B with ± 45 rastering and Z print direction.

(d) Results from the Topology Optimization process of Part B with 0/90 rastering and X print direction.
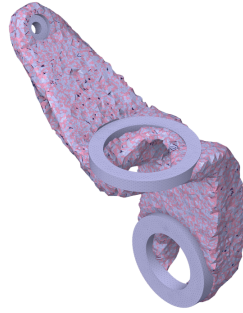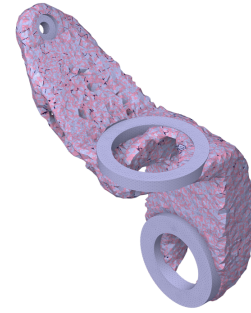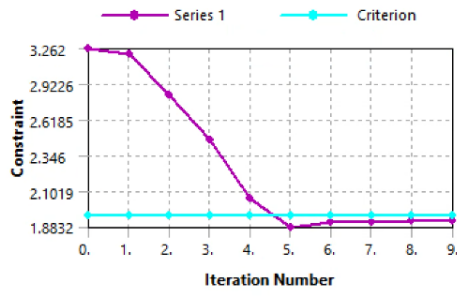

(e) Results from the Topology Optimization process of Part B with 0/90 rastering and Y print direction.
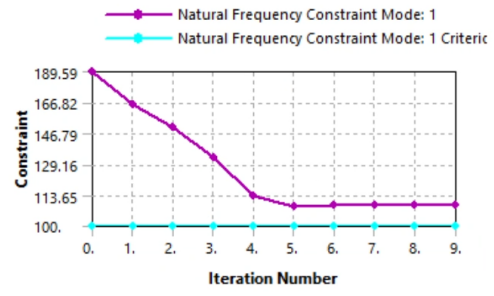

(f) Results from the Topology Optimization process of Part B with 0/90 rastering and Z print direction.

Figure 33: The results from the Topology Optimization process of Part B.

A selection of the mass and natural frequency values, as they change with the iterations, can be seen in Figure 34. While all the mass and natural frequency data can be seen in Figure 35.

(a) The change in mass for Part A with 0/90 rastering and X print direction.

(b) The change in natural frequency for Part A with 0/90 rastering and X print direction.
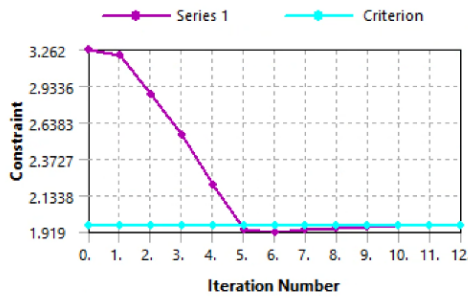
(c) The change in mass for Part A with 0/90 rastering and Z print direction.
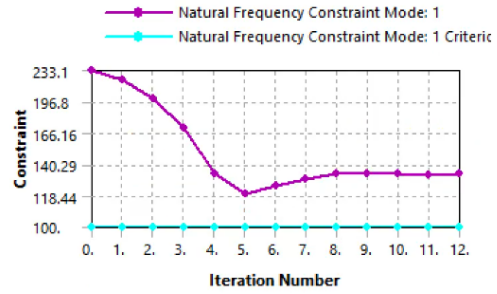
(d) The change in natural frequency for Part A with 0/90 rastering and Z print direction.

Figure 34: A selection of the change in mass and natural frequency during the topology optimization process for Part A.
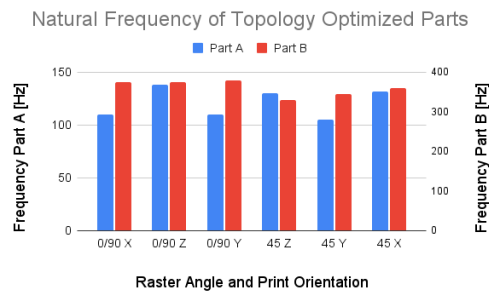
(a) The natural frequency of the different results from the TO process.
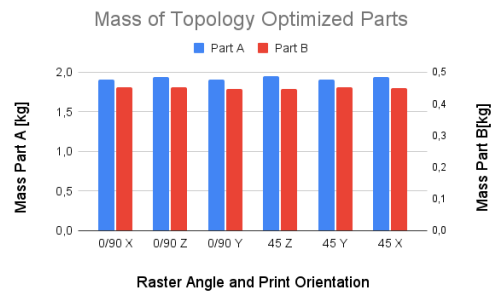
(b) The mass of the different results from the TO process.

Figure 35: The natural frequency and mass of the final iteration from the different TO processes.

6.4   Discussion

We see that the TO results are nearly identical, independent of the simulated print direction. All the results had a mass very close to 60% of the original mass as the algorithm tried to maximize the stiffness of the part, not reduce the mass. It was observed that the mass would reach 60% after just a few iterations, and then the remaining iterations would hold the mass constant while decreasing the compliance of the part. This is also possible to see from the natural frequency constraint. At the start it would decrease quickly before stabilizing and then slowly increase again.

The results show that using materials with anisotropic properties in a topology optimization process is possible. While the mass and geometry of the different simulations are very similar to each other, the natural frequency varied more as seen in Figure 35. This is expected as the objective function only valued decreasing the compliance of the part, not the mass. So the optimal solution had the maximum mass allowed by the mass constraint while trying to increase the stiffness of the part. The anisotropic properties of the material resulted in different natural resonant frequencies.

7   Conclusion

Using FDM printed components to produce satellite components allows for more freedom in the design process. The anisotropic properties do, however, pose a challenge when modelling the material, but they also provide opportunities for more optimized parts. The increased strength in specific directions can be exploited to reduce the mass in unnecessary places. Support structures might need to be utilized to capitalize on the capability to produce complex geometries fully. The results showed little to no effect of support structures on the strength of the parts. This is helpful when designing parts as the designer does not need to spend time creating designs without overhangs. However, support structures do decrease the surface finish and require manual work to be removed, so overhangs should not be used if it is an option.

The cyclic loading behaviour of satellite components is vital due to the large amount of vibrations during launch. The results from the cyclic testing showed that with $R = -1$ the stress amplitude should be kept relatively low to survive the launch. It was speculated that the reason for the poor fatigue life is that the high loading frequency caused heating in the component that degraded the strength. So when designing satellite components cyclic stress during the launch might be a constraining factor.

Topology optimization used in conjunction with FDM manufacturing is certainly possible, and it is possible to include some of the anisotropic properties in the topology optimization process. It was shown that the mass and general geometry of the components stayed similar independent of the simulated print direction. But the natural frequency did vary significantly, indicating that the anisotropic properties caused by the FDM manufacturing did affect the TO process. Different constraints and objective functions could probably achieve a different mass and geometry.

The workflow used to determine the mechanical properties of FDM manufactured components gave good results. It was possible to reproduce the observed strains in the load direction, resulting in a good correlation between the experimental and validated estimates of Young's Modulus. The Poisson's ratios however were less predictable, so to understand the strains in the direction perpendicular to the loading, further research has to be done.

8 Further research

To further the understanding of the use of PEEK for satellite components, more experiments with cyclic loading could be conducted. A key omission from the data recorded during the cyclic loading tests was the samples' temperature. Additional tests at different stress ratios and loading frequencies, while recording the temperature could be useful. Testing samples with removed support structures in cyclic loading could be interesting as the rougher surface finish could affect the performance more in cyclic loading than static tensile tests.

Investigating the shear strength and modulus could also offer better insight into the anisotropic properties of FDM manufactured components and PEEK. This could be done using the methodology described by *Rohde et al.* [33].

Further work could also be done in the topology optimization part of the process. Different constraints and objective functions could be used to see if they result in the print direction affecting the results more significantly. In addition, it could be interesting to see the effect of the use of manufacturing constraints such as a maximum overhang. However, due to the low impact on strength by the support structures, this is less interesting.

Bibliography

[1] Jonathan McDowell. *General Catalog of Artificial Space Objects*. URL: https://planet4589.org/space/gcat/data/derived/launchlog.html (visited on 26th June 2022).

[2] Byron Blakey-Milner et al. 'Metal additive manufacturing in aerospace: A review'. In: *Materials & Design* 209 (Nov. 2021), p. 110008. ISSN: 02641275. DOI: 10.1016/j.matdes.2021.110008. URL: https://linkinghub.elsevier.com/retrieve/pii/S0264127521005633 (visited on 14th Aug. 2022).

[3] Michel Capderou. *Satellites - orbits and missions*. en. Berlin Heidelberg: Springer, 2005. ISBN: 978-2-287-21317-5.

[4] SpaceX. *Falcon User's Guide*. Sept. 2021. URL: https://www.spacex.com/media/falcon-users-guide-2021-09.pdf.

[5] THE AUSTRALIAN SPACE WEATHER AGENCY. 'SatelliteOrbitalDecayCalculations'. In: (), p. 11.

[6] Fredrick Madaraka Mwema and Esther Titilayo Akinlabi. *Fused Deposition Modeling: Strategies for Quality Enhancement*. SpringerBriefs in Applied Sciences and Technology. Cham: Springer International Publishing, 2020. ISBN: 978-3-030-48258-9 978-3-030-48259-6. DOI: 10.1007/978-3-030-48259-6. URL: http://link.springer.com/10.1007/978-3-030-48259-6 (visited on 14th Aug. 2022).

[7] Harshit K. Dave and J. Paulo Davim, eds. *Fused Deposition Modeling Based 3D Printing*. Materials Forming, Machining and Tribology. Cham: Springer International Publishing, 2021. ISBN: 978-3-030-68023-7 978-3-030-68024-4. DOI: 10.1007/978-3-030-68024-4. URL: https://link.springer.com/10.1007/978-3-030-68024-4 (visited on 14th Aug. 2022).

[8] Prusa. *Supported file formats*. Supported file formats. 13th Aug. 2021. URL: https://help.prusa3d.com/article/supported-file-formats_1772 (visited on 13th Aug. 2022).

[9] Georg Aarnes Nisja, Anni Cao and Chao Gao. 'Short review of nonplanar fused deposition modeling printing'. In: *Material Design & Processing Communications* 3.4 (Aug. 2021). ISSN: 2577-6576, 2577-6576. DOI: 10.1002/mdp2.221. URL: https://onlinelibrary.wiley.com/doi/10.1002/mdp2.221 (visited on 14th Aug. 2022).

[10] Martin Lütkemeyer. *3D Printer Line/Extrusion Width — Best Settings & Examples*. URL: https://the3dprinterbee.com/3d-printer-line-extrusion-width/ (visited on 13th Aug. 2022).

[11] Martin Lütkemeyer. *3D Printing Layer Height vs. Nozzle Size – Table & Guide*. URL: https://the3dprinterbee.com/3d-printer-line-extrusion-width/ (visited on 13th Aug. 2022).

[12] Adi Pandzic, Damir Hodzic and Aleksa Milovanovic. 'Effect of Infill Type and Density on Tensile Properties of PLA Material for FDM Process'. In: *DAAAM Proceedings*. Ed. by Branko Katalinic. 1st ed. Vol. 1. DAAAM International Vienna, 2019, pp. 0545–0554. ISBN: 978-3-902734-22-8. DOI: 10.2507/30th.daaam.proceedings.074. URL: http://www.daaam.info/Downloads/Pdfs/proceedings/proceedings_2019/074.pdf (visited on 14th Aug. 2022).

[13] Razieh Hashemi Sanatgar, Christine Campagne and Vincent Nierstrasz. 'Investigation of the adhesion properties of direct 3D printing of polymers and nanocomposites on textiles: Effect of FDM printing process parameters'. In: *Applied Surface Science* 403 (May 2017), pp. 551–563. ISSN: 01694332. DOI: 10.1016/j.apsusc.2017.01.112. URL: https://linkinghub.elsevier.com/retrieve/pii/S0169433217301137 (visited on 14th Aug. 2022).

[14] Jasgurpreet Singh Chohan and Rupinder Singh. 'Pre and post processing techniques to improve surface characteristics of FDM parts: a state of art review and future applications'. In: *Rapid Prototyping Journal* 23.3 (18th Apr. 2017), pp. 495–513. ISSN: 1355-2546. DOI: 10.1108/RPJ-05-2015-0059. URL: https://www.emerald.com/insight/content/doi/10.1108/RPJ-05-2015-0059/full/html (visited on 14th Aug. 2022).

[15] Syed A.M. Tofail et al. 'Additive manufacturing: scientific and technological challenges, market uptake and opportunities'. In: *Materials Today* 21.1 (Jan. 2018), pp. 22–37. ISSN: 13697021. DOI: 10.1016/j.mattod.2017.07.001. URL: https://linkinghub.elsevier.com/retrieve/pii/S1369702117301773 (visited on 14th Aug. 2022).

[16] Evangelos Tyflopoulos et al. 'Simulation-based design: a case study in combining optimization methodologies for angle-ply composite laminates'. In: *Procedia CIRP* 100 (2021), pp. 607–612. ISSN: 22128271. DOI: 10.1016/j.procir.2021.05.131. URL: https://linkinghub.elsevier.com/retrieve/pii/S2212827121006053 (visited on 31st Aug. 2022).

[17] Ole Sigmund and Kurt Maute. 'Topology optimization approaches: A comparative review'. In: *Structural and Multidisciplinary Optimization* 48.6 (Dec. 2013), pp. 1031–1055. ISSN: 1615-147X, 1615-1488. DOI: 10.1007/s00158-013-0978-6. URL: http://link.springer.com/10.1007/s00158-013-0978-6 (visited on 31st Aug. 2022).

[18] Lorna J Gibson. *Cellular solids : structure and properties*. eng. Cambridge, 1997.

[19] Evangelos Tyflopoulos, Cecilia Haskins and Martin Steinert. 'Topology-Optimization-Based Learning: A Powerful Teaching and Learning Framework under the Prism of the CDIO Approach'. In: *Education Sciences* 11.7 (13th July 2021), p. 348. ISSN: 2227-7102. DOI: 10.3390/educsci11070348. URL: https://www.mdpi.com/2227-7102/11/7/348 (visited on 31st Aug. 2022).

[20] Piaras Kelly. *Solid Mechanics Lecture Notes*. URL: http://homepages.engineering.auckland.ac.nz/~pkel015/SolidMechanicsBooks/index.html.

[21] Parina Patel et al. 'Mechanism of thermal decomposition of poly(ether ether ketone) (PEEK) from a review of decomposition studies'. In: *Polymer Degradation and Stability* 95.5 (May 2010), pp. 709–718. ISSN: 01413910. DOI: 10.1016/j.polymdegradstab.2010.01.024. URL: https://linkinghub.elsevier.com/retrieve/pii/S0141391010000340 (visited on 14th Aug. 2022).

[22] Joachim Rösler, Harald Harders and Martin Bäker. *Mechanisches Verhalten der Werkstoffe: mit 31 Tabellen und 34 Aufgaben und Lösungen*. 2., durchges. und erw. Aufl. Lehrbuch Maschinenbau. Wiesbaden: Teubner, 2006. 521 pp. ISBN: 978-3-8351-0008-4.

[23] NASA. *Outgassing Data PEEK (POLYETHERRTHERKEYTONE)*. GSFC30151. 2007. URL: https://outgassing.nasa.gov/outgassing-data-table?field_material_value_op=starts&field_material_value=PEEK&field_application_value_op=contains&field_application_value=Machinable (visited on 5th June 2022).

[24] 'TECAFIL PEEK VX CF30 black - Filament'. In: (), p. 1. URL: https://www.ensinger-online.com/modules/public/sheet/createsheet.php?SID=3241&FL=0&FILENAME=TECAFIL_PEEK_VX_CF30_black_0.PDF&ZOOM=0.7.

[25] Ensinger. *TECAFIL PEEK VX CF30 black 1,75 mm - 500g*. 2022. URL: https://filaments.ensingerplastics.com/products/carbon-fiber-peek-filament-tecafil-peek-vx-cf30-black-1-75-mm-500g.

[26] SN/K 138. *NS-EN ISO 527*. 1st Dec. 2019.

[27] Olav Bjørken, Christer W. Elverum and Martin Steinert. 'TMM4960-MastersThesis2022-OUB.pdf'. PhD thesis. NTNU. (Visited on 31st July 2022).

[28] E08 Committee. *Practice for Conducting Force Controlled Constant Amplitude Axial Fatigue Tests of Metallic Materials*. ASTM International. DOI: 10.1520/E0466-15. URL: http://www.astm.org/cgi-bin/resolver.cgi?E466-15 (visited on 22nd Aug. 2022).

[29] Andreas Hagerup Birkelid et al. 'High-performance polymer 3D printing – Open-source liquid cooled scalable printer design'. In: *HardwareX* 11 (Apr. 2022), e00265. ISSN: 24680672. DOI: 10.1016/j.ohx.2022.e00265. URL: https://linkinghub.elsevier.com/retrieve/pii/S2468067222000104 (visited on 14th Aug. 2022).

[30] Aprium. *Apium P220*. URL: https://apiumtec.com/en/industrial-3d-printer (visited on 22nd Aug. 2022).

[31] correlated Solutions. *Vic-2D v6 Reference Manual*. (Visited on 26th July 2022).

[32] Li et al. 'Flexural Properties and Fracture Behavior of CF/PEEK in Orthogonal Building Orientation by FDM: Microstructure and Mechanism'. In: *Polymers* 11.4 (10th Apr. 2019), p. 656. ISSN: 2073-4360. DOI: 10.3390/polym11040656. URL: https://www.mdpi.com/2073-4360/11/4/656 (visited on 19th Aug. 2022).

[33] S. Rohde et al. 'Experimental Characterization of the Shear Properties of 3D–Printed ABS and Polycarbonate Parts'. In: *Experimental Mechanics* 58.6 (July 2018), pp. 871–884. ISSN: 0014-4851, 1741-2765. DOI: 10.1007/s11340-017-0343-6. URL: http://link.springer.com/10.1007/s11340-017-0343-6 (visited on 28th Aug. 2022).